The Experimental HWRF System: A Study on the Influence of Horizontal Resolution on the Structure and Intensity Changes in Tropical Cyclones Using an Idealized Framework

SUNDARARAMAN G. GOPALAKRISHNAN AND FRANK MARKS JR.

NOAA/Hurricane Research Division/Atlantic Oceanographic Meteorological Laboratory, Miami, Florida

XUEJIN ZHANG

Cooperative Institute for Marine and Atmospheric Studies, University of Miami, Miami, Florida

JIAN-WEN BAO

NOAA/Earth System Research Laboratory, Boulder, Colorado

KAO-SAN YEH

Cooperative Institute for Marine and Atmospheric Studies, University of Miami, Miami, Florida

ROBERT ATLAS

Atlantic Oceanographic Meteorological Laboratory, Miami, Florida

(Manuscript received 8 June 2010, in final form 31 August 2010)

ABSTRACT

Forecasting intensity changes in tropical cyclones (TCs) is a complex and challenging multiscale problem. While cloud-resolving numerical models using a horizontal grid resolution of 1–3 km are starting to show some skill in predicting the intensity changes in individual cases, it is not clear at this time what may be a reasonable horizontal resolution for forecasting TC intensity changes on a day-to-day-basis. The Experimental Hurricane Weather Research and Forecasting System (HWRFX) was used within an idealized framework to gain a fundamental understanding of the influence of horizontal grid resolution on the dynamics of TC vortex intensification in three dimensions. HWFRX is a version of the National Centers for Environmental Prediction (NCEP) Hurricane Weather Research and Forecasting (HWRF) model specifically adopted and developed jointly at NOAA's Atlantic Oceanographic and Meteorological Laboratory (AOML) and Earth System Research Laboratory (ESRL) for studying the intensity change problem at a model grid resolution of about 3 km. Based on a series of numerical experiments at the current operating resolution of about 9 km and at a finer resolution of about 3 km, it was found that improved resolution had very little impact on the initial spinup of the vortex. An initial axisymmetric vortex with a maximum wind speed of 20 m s^{-1} rapidly intensified to 50 m s^{-1} within about 24 h in either case. During the spinup process, buoyancy appears to have had a pivotal influence on the formation of the warm core and the subsequent rapid intensification of the modeled vortex. The high-resolution simulation at 3 km produced updrafts as large as 48 m s^{-1}. However, these extreme events were rare, and this study indicated that these events may not contribute significantly to rapid deepening. Additionally, although the structure of the buoyant plumes may differ at 9- and 3-km resolution, interestingly, the axisymmetric structure of the simulated TCs exhibited major similarities. Specifically, the similarities included a deep inflow layer extending up to about 2 km in height with a tangentially averaged maximum inflow velocity of about 12–15 m s^{-1}, vertical updrafts with an average velocity of about 2 m s^{-1}, and a very strong outflow produced at both resolutions for a mature storm. It was also found in either case that the spinup of the primary circulation occurred not only due to the weak inflow above the boundary layer but also due to the convergence of vorticity within the boundary layer. Nevertheless, the mature phase of the storm's evolution exhibited significantly different patterns of behavior at 9 and 3 km. While the minimum pressure at the end of 96 h was 934 hPa for the 9-km simulation, it was about 910 hPa for the 3-km run. The maximum tangential wind at that time showed a difference of about 10 m s^{-1}. Several sensitivity experiments related to the initial vortex intensity, initial radius of the maximum wind, and physics were performed. Based on ensembles of simulations, it appears that radial advection of the tangential wind and, consequently, radial flux of vorticity become important forcing terms in the momentum budget of the mature storm. Stronger convergence in the boundary layer leads to a larger transport of moisture fluxes and, subsequently, a stronger storm at higher resolution.

Corresponding author address: S. G. Gopalakrishnan, AOML/HRD, 4301 Rickenbacker Cswy., Miami, FL 33149.
E-mail: gopal@noaa.gov

DOI: 10.1175/2010MWR3535.1

1. Introduction

Forecasting intensity changes in tropical cyclones (TCs) is a complex and challenging problem. The factors that are known to influence these changes vary in scale ranging from several hundreds of kilometers (e.g., environmental shear, dry air, and upper-ocean structure) to a few kilometers (e.g., vortex and convective-scale asymmetries and ocean waves) and, sometimes, even down to a few hundred meters (e.g., wind gusts, aerosols, and microphysical processes). The Experimental Hurricane Weather Research and Forecasting System (HWRFX) is a version of the National Centers for Environmental Prediction (NCEP) Hurricane Weather Research and Forecasting (HWRF) system specifically adopted and developed at the Hurricane Research Division of the Atlantic Oceanographic and Meteorological Laboratory and Earth System Research Laboratory to study the intensity change problem at the finest model grid resolution feasible at this time for forecasting. In this paper, we seek a fundamental understanding of the intensification process of an initially cloud-free, axisymmetric, baroclinic vortex on an *f* plane in a shear-free environment over a warm ocean with fixed sea surface temperatures in a weak easterly current of 4 m s^{-1} (henceforth the ideal vortex) using the HWRFX system.

Past studies, starting with the pioneering theoretical work of Riehl (1954), Ooyama (1969, 1982), and Emanuel (1986), supported with inner-core observations (Willoughby 1979, 1990a,b), have all led to a well-accepted understanding of the axisymmetric inner-core structure and evolution of the TC. In a shear-free, semi-ideal environment, the intensification of TCs occurs by means of cooperative interaction between the primary and secondary circulation patterns. While the tangential wind (i.e., along the tangential direction in the cylindrical polar coordinate system) constitutes the primary circulation and angular momentum is approximately conserved above the boundary layer in this direction, the secondary circulation includes the radial inflow, upward motion, outflow, diabatic and, to some extent, adiabatic heating in the mid- to upper troposphere; and the subsequent core warming (Riehl 1954; Ooyama 1982). Typically, the warm core is supported by the evaporation and sensible heat supply from the warm ocean and inward enthalpy flux in the boundary layer. Furthermore, when the near-surface heat and moisture fluxes are transported upward by the secondary circulation, cumulus convection being the agent, a continual positive feedback is produced between the upward transport of near-surface fluxes, the deepening of pressure gradients primarily between the center and the eyewall, and the further increase in wind near the surface and deeper layer of the atmosphere until an equilibrium is attained (Emanuel 1986). As indicated by observational analysis (e.g., Willoughby 1990b) and some earlier models (e.g., Sundqvist 1970), the gradient wind relationship also holds fairly well above the boundary layer in mature TCs. Several axisymmetric models have been developed to understand the intensity changes in TCs (e.g., Yamasaki 1977; Kurihara 1975). A detailed review of the earlier works until 1967 is provided in Ooyama (1969). A review of more recent findings and a century of scientific progress in understanding the hurricane problem is reported in Emanuel (2003).

It should be noted that in all of the above studies the evolution of the axisymmetric vortex is composed of a rapidly evolving phase followed by a mature stage where the intensification is slow (e.g., Figs. 2 and 3 in Sundqvist 1970). While axisymmetric models may be able to explain rapid intensification to some extent and slow evolution to a larger extent, especially when the vortex is neutral to slantwise convection (Rotunno and Emanuel 1987), as shown in our present work and that of Nguyen et al. (2008) and Montgomery et al. (2009), rapidly intensifying tropical cyclones are highly asymmetric. It is not clear how these asymmetries may influence the initial evolution of the storm. For instance, Rotunno and Emanuel (1987) explained the evolutionary phase of the storm as follows: ''As the vortex wind passes over the ocean surface, equivalent potential temperature θ_e is transferred to the interior and leads locally to conditional instability, cumulus convection, and subsequent precipitation.'' While their conclusions may be correct for the case under consideration, the implicit assumption is that convection is symmetric around the eyewall region. Axisymmetric models also have limited applications for the forecasting problem.

Over the past 20 yr, significant advances have been made in the numerical prediction of TCs. Much of this progress is due to advances in the development of three-dimensional models that approximate the fluid motion of the atmosphere to create forecasts of the weather at some time in the future. Since 1995, the Geophysical Fluid Dynamic Laboratory's (GFDL) hydrostatic hurricane prediction system has been used operationally by the National Hurricane Center (NHC) and has proved to be the first numerical model to beat statistical models in track forecast skill. It has recently illustrated improved skill in intensity predictions, especially with increases in vertical and horizontal resolution (Bender et al. 2007). Apart from forecasting, a version of this modeling system has also been used for the purpose of understanding the hurricane problem (e.g., Kurihara and Tuleya 1974; Tuleya and Kurihara 1975, 1978, 1982; Shen et al. 2000). For instance, Kurihara and Tuleya (1974) used an 11-level

primitive equation model with a horizontal resolution of about 20 km near the eye of the storm and studied the structure and development of an idealized TC in three dimensions. They obtained intensity changes and an axisymmetric structure consistent with our current understanding of TCs. They also found that the energy and angular momentum budgets are primarily controlled by the axisymmetric mean around the vortex (Tuleya and Kurihara 1975). Nevertheless, the hurricane intensity change problem is a multiscale problem and, as seen later in this text, may require cloud-scale resolutions (of 1–3 km) for simulating and understanding the inner-core processes (Rogers 2010). The Hurricane Weather Research and Forecasting (HWRF) system is a high-resolution, nonhydrostatic forecast system developed at NCEP's Environmental Modeling Center (EMC) to address the intensity change problem (information online at http://www.emc.ncep.noaa.gov/HWRF/index.html). This system is expected to replace the GFDL modeling system.

Cloud-resolving models have been used by the research community to understand the TC intensity change problem. In a series of explicit simulations, the fifth-generation Pennsylvania State University–National Center for Atmospheric Research (PSU–NCAR) Mesoscale Model (MM5) at a resolution of about 1.67 km was used to examine the basic process of intensification of an idealized vortex (Nguyen et al. 2008; Montgomery et al. 2009; Smith et al. 2008, 2009). Their studies point out that (i) the intensification process is asymmetric and vortical hot towers may be an intensification pathway (Nguyen et al. 2008; Montgomery et al. 2009) and (ii) the axisymmetric aspects of intensification involve not only the convergence of absolute angular momentum above the boundary layer but also the convergence of absolute angular momentum within the boundary layer. The latter is aided by supergradient winds (Smith et al. 2008, 2009). In the current work, we use the HWRFX system to provide new and additional insights into the idealized vortex intensification problem. Specifically, we seek to answer the following questions: (i) Does the new forecasting system produce the fundamental features of vortex spinup consistent with some of the observations and theoretical works mentioned above? (ii) What is the role of convective asymmetries on the initial intensification of the storm? (iii) What is the impact of model grid resolution on the evolution of the TCs? To the best of our knowledge, this is the first extensive effort that objectively investigates the effects of model grid resolution on the rapid intensity change in TCs and the subsequent evolution of the matured storm. We also believe that the third aspect of this problem may be useful to the forecasting community as well. In the next section, we provide a brief summary of the model dynamics, especially the moving telescopic grid, because it has not been reported elsewhere. Section 2b deals with model configurations, initial conditions, and physics. Section 2c describes the methodology of analysis of the results. We discuss the results in section 3 and provide our conclusions in section 4.

2. The modeling system and analysis

a. The HWRFX moving nested grid system

A novel numerical approach (Janjić et al. 2001; Janjić 2003) was applied to the NCEP Nonhydrostatic Mesoscale Model (NMM) that is currently a dynamical core option within the Weather Research and Forecasting (WRF) model initiative. With this approach, instead of extending cloud models to larger spatial and temporal scales, the hydrostatic approximation is relaxed in a hydrostatic system of equations so as to extend the applicability of the model to nonhydrostatic motions. At the same time, the favorable features of the hydrostatic formulation are preserved within the range of validity of the hydrostatic approximation. The NMM-WRF nonhydrostatic system of equations is formulated on a rotated latitude–longitude Arakawa E grid, while in the vertical a pressure–sigma hybrid coordinate is used. The latitude–longitude coordinate is simply transformed in such a way that the coordinate origin is located in the center of the integration domain. This kind of transformation provides a more uniform grid size all over the domain and, consequently, avoids the need for an excessively small time step as the model boundaries approach the northern–southern latitudes. The dynamical system of equations and the numerical techniques are described for a uniform domain in Janjić et al. (2001) and Janjić (2003). The HWRFX uses the same dynamics as the WRF-NMM system. To deal with TC forecasting, a horizontal mesh refinement capability was developed for this dynamical core. The refinement capability commonly referred to as telescopic mesh supports one- and two-way interaction between a lower-resolution parent domain and one or more higher-resolution nests.

All interpolations from the parent to the nested domain are performed on a rotated latitude–longitude E grid with the reference latitude–longitude located at the center of the parent domain (Fig. 1a). Consequently, the nested domain can be freely moved anywhere within the grid points of the parent domain, yet the nested domain latitude–longitude lines will coincide with the latitude–longitude lines of the parent domain at an integer parent-to-nest grid-size ratio (Fig. 1b). Terrain is an important forcing term in the dynamics of hurricane

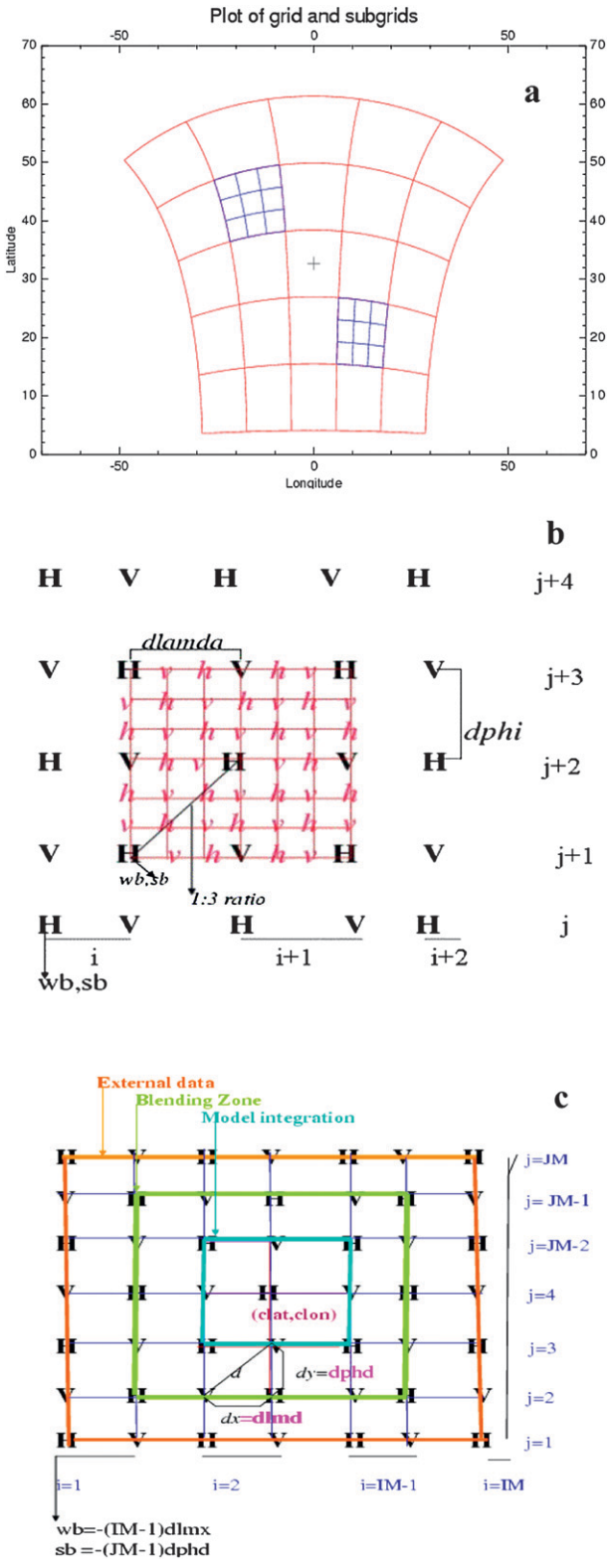

FIG. 1. Moving nest configuration. (a) The HWRFX telescopic nest as it appears on a true latitude–longitude coordinate system. (b) The nested E-grid configuration for a 3:1 parent-to-nest ratio. Here, "wb" and "sb" are the western and southern boundaries, respectively. The NMM grid indexing is also shown for the parent domain where "im" and "jm" are the maximum *i* and *j* indices, respectively. (c) The nested boundary conditions showing the grid index. External data in this case are obtained from the parent domain at every parent-domain time step. Here, *d* is the nearest distance between two mass or velocity points and lies along the diagonal. Additionally, dlamda and dphd are equivalent to *dx* and *dy* but in degrees. Please note that this is a highly truncated grid configuration. In practice the parent and the nested domains span many more grid points.

forecasting. Careful treatment of static terrestrial conditions is necessary to avoid contamination and possible noise in the modeled solution due to improper adjustment between mass and high-resolution terrestrial information. The WRF Preprocessor (WPS) is used to generate terrain datasets over multiple domains at the required grid resolution. For instance, in a typical operational forecast at 27 km with a moving nest at 9-km resolution, terrestrial data are generated at both of the resolutions for the entire parent domain shown in Fig. 1a. The nested domain does not use any of the terrain information from the parent domain and, subsequently, pressure information is not directly interpolated from the hybrid surfaces of the parent domain onto the high-resolution nested domain either. The height, temperature, and moisture fields from the parent domain are vertically interpolated onto standard pressure surfaces. The above meteorological fields from the parent domain are further interpolated in the horizontal direction onto the nested grid on the same pressure surface. Finally, by using high-resolution topography over the nested domain, hydrostatic mass balancing is carried out to prescribe the initial values in the nested domain. The surface pressure, interface pressure, hydrostatic surface pressure, temperature, and moisture are recovered on the hybrid surfaces of the nested domain by using cubic spline interpolation. This approach seems to be simple yet produces an effective way of initializing the nested domain and updating the interface for the initial conditions without much distortion or noise, even while moving the telescopic nest. Simple bilinear interpolation is used for initializing all meteorological fields in the horizontal. The nearest-neighbor approach is adopted for prescribing most of the land state variables. For the current idealized study, the terrain is set to zero.

Figure 1c illustrates a sample E-grid structure with the outermost rows and columns representing the external interface. The fine grid data at this interface are prescribed by downscaling the coarse grid data at every time step of the parent domain (i.e., interpolation and hydrostatic adjustment mentioned above). Fine-grid

integration starts from the third internal column/row, which is called the dynamic interface in the figure. The data in the penultimate rows and columns are a blend of prescribed and dynamic interfaces. While bilinear interpolation from the parent onto the nested domain is used to prescribe the wind and the total condensate, the mass adjustment procedure adopted for initialization is repeated, but this time only at the outermost boundaries. This approach is a simple, yet effective technique for updating the interface without excessive distortion or noise. For the two-way interactive technique, nine-point-averaged mass, momentum, and scalar fields from the high-resolution nest are weighed and fed back into the parent domain. Currently, the weighting factor is 0.5.

The nest motion for the TCs is based on the concept of dynamic pressure (Gopalakrishnan et al. 2002). At the end of every time step of the nested domain, the dynamic pressure within this domain is determined. The minimum dynamic pressure determines the storm center. If the storm center is advected beyond one grid point of the parent domain (three grid points from the center of the nested domain for a 3:1 parent-to-nest grid ratio that is usually used), the nested domain is moved to a new position within the parent domain to maintain the storm at the center of the nested domain. The nested domain cannot be moved by more than two parent domain grid points at a particular time step. While data are exchanged at a given time step before and after the grid motion in most parts of the domain (i.e., modified through the revision of horizontal indices), the interpolation and hydrostatic balancing procedures discussed earlier are applied to the leading edge of the moving nest (where there are no data to exchange). Additionally, if the pressure difference between the center and the point of maximum dynamic pressure is less than 2 hPa, the grid motion is terminated. This nest motion algorithm has been routinely used in the operational version of the HWRF system since 2006. If a storm is successfully located initially (i.e., at the start of a forecast) somewhere within the nested domain, the algorithm is sufficiently robust to provide automatic grid motion at subsequent times.

b. *Configuration, model physics, and initial conditions*

The domain of the simulation along the horizontal direction was set to about $50° \times 50°$ with a moving nest of about $8° \times 8°$. There were 40 hybrid levels along the vertical with the top level set to 50 hPa. The simulations reported here were run with two kinds of horizontal resolution, namely, (i) a parent domain at a resolution of about 27 km with a 9-km moving nest (hereinafter 27:09) and (ii) a parent domain at a resolution of 9 km with a moving nest at 3 km (hereinafter 09:03). While the former was designed to be consistent with the current operational resolution, the latter could be the possible choice in the near future. All the results reported in this work are products from the moving nest at either 9- or 3-km resolution. The model was run for 96 h (4 days).

As discussed in Yeh et al. (2010, manuscript submitted to *J. Nat. Hazards*) the physics options used here are configured as closely as possible to the operational HWRF system. The so-called GFDL surface and boundary layer formulations are used to parameterize the flux transport and the subsequent mixing in the atmosphere. The Ferrier scheme is used to provide latent heating due to the microphysical processes in the atmosphere, and the simplified Arakawa and Schubert scheme (SAS) is used to parameterize subgrid cumulus-cloud activity. Cumulus parameterization (e.g., Pan and Wu 1995), in combination with the Ferrier microphysical scheme, have been found to have some value in operational models at scales down to less than 5 km. However, the contribution to heating from SAS has diminishing returns, that is, an increase in resolution and the grid volume in the inner-core region quickly becoming saturated with the use of an explicit microphysics scheme alone. To maintain consistency in the comparison of our results at 9 and 3 km, we retain the SAS convection scheme at 3-km resolution as well. Nevertheless, we have performed a sensitivity experiment without SAS convection at 3-km resolution, which is reported upon in section 3. Finally, to keep the radiation option simple, the effects of radiation on the atmosphere are approximated with the NCAR long- and shortwave radiation scheme available within the WRF framework. Detailed descriptions of the physics options in HWFX with appropriate references are reported in Yeh et al. (2010, manuscript submitted to *J. Nat. Hazards*).

A full description of the idealized vortex initialization procedure for the HWRFX will be provided in a complementary publication (J.-W. Bao 2010, personal communication). In brief, the nonlinear balance equation in the pressure-based sigma coordinate system described in Wang (1995) was solved within the rotated latitude–longitude E-grid framework, where the mass field was obtained from the wind field. The model is initialized with an axisymmetric cyclonic vortex embedded in a uniform easterly flow of 4 m s^{-1}. The far-field temperature and humidity are based on Jordan's Caribbean sounding (Gray et al. 1975). In all of the experiments, the sea surface temperature was set to 302 K. Several experiments were performed at 27:09 and 09:03 with different configurations of the ideal vortex and are reported in Table 1.

TABLE 1. List of experiments performed at 9- and 3-km resolutions.

No.	Description	Initial vortex strength (m s^{-1})	Convection scheme for the 3-km nest	Initial radius of max wind (km)	Specification
1	Control	20	Yes	90	C09, C03
2	Strong	30	Yes	90	S09, S03
3	R0	20	Yes	120	R09, R03
4	No SAS	20	No	90	SAS09, SAS03

Although the physics options in HWRFX were kept as closely as possible to the operational physics, apart from the difference in the radiation scheme, there were several subtle but significant changes adopted in this ideal case study. As pointed out by one of the reviewers, we believe that it may be worthwhile to contrast these differences. Fortunately, the operational suite of physics has been recently published as a technical document at NCAR's Development Testbed Center. This documentation is coauthored by Gopalakrishnan et al. (2010; information online at http://www.dtcenter.org/HurrWRF/users/docs/scientific_documents/HWRF_final_2-2_cm.pdf and http://www.dtcenter.org/HurrWRF/users/online_tutorial/tutorial02222010.php). In Table 2, we specify some main differences in the physics between the control simulation (C09) and the operational HWRF physics.

c. Methodology of analysis of the results

Apart from time traces of minimum mean sea level pressure and 10-m wind speeds in the core that were simply isolated from the raw hourly output on the native grid system, we divided our analysis into two parts. The first part deals with instantaneous model outputs that were taken at an interval of 6 min on the native grid and interpolated onto a height coordinate system. The instantaneous output was used to perform a qualitative study of the development of the warm core between hours 0 and 24 in C09 and C03 (Table 1). The second part deals with the axisymmetric mean created from hourly outputs for the entire period of the simulation. As illustrated in Liu et al. (1999) and Zhang et al. (2001), it is convenient to discuss the axisymmetric inner-core dynamics in cylindrical coordinates (r, λ, z), where r is the distance from the center of the vortex, λ is the azimuthal angle, and z is the vertical height. The hourly output on the native grid from the model was transformed to the cylindrical polar height coordinate system. Further, for the sake of our analysis, we recast the horizontal equations of motion into radial and tangential momentum components similar to the work of Zhang et al. (2001) but in a simplified form appropriate for the HWRFX system. We provide these equations below:

$$\frac{du_r}{dt} = \underbrace{-\frac{1}{\rho}\frac{\partial p}{\partial r} + \frac{v_\lambda v_\lambda}{r} + fv_\lambda}_{\text{TermA}} + Du_r \quad \text{and} \tag{1}$$

$$\frac{dv_\lambda}{dt} = -\frac{1}{\rho r}\frac{\partial p}{\partial \lambda} - \underbrace{\frac{u_r v_\lambda}{r} - fu_r}_{\text{TermB}} + Dv_\lambda, \tag{2}$$

$$\text{where} \quad \frac{d}{dt} = \frac{\partial}{\partial t} + u_r\frac{\partial}{\partial r} + \frac{v_\lambda}{r}\frac{\partial}{\partial \lambda} + w\frac{\partial}{\partial z}. \tag{3}$$

In Eqs. (1)–(3), u_r, v_λ, and w are, respectively, the radial, tangential, and vertical winds in the earth-relative transformed coordinate system; p is the pressure; and

TABLE 2. List of differences between operational HWRF and HWRFX physics for the idealized configuration at 27:09 (i.e., C09 configuration).

	Grid configuration	Convection	Microphysics	Boundary and surface layers	Dissipative heating	Radiation
Operational HWRF	Two grids, 27/9 km	SAS with momentum mixing	Ferrier	GFS boundary layer and GFDL hurricane model surface layer scheme (with modification to surface roughness)	Switched on	GFDL radiation scheme
HWRFx C09	Two grids, 27/9 km	SAS without momentum mixing	Ferrier	GFS boundary layer and GFDL hurricane model scheme with the original Charnock approximation for surface roughness	Switched off	NCAR package

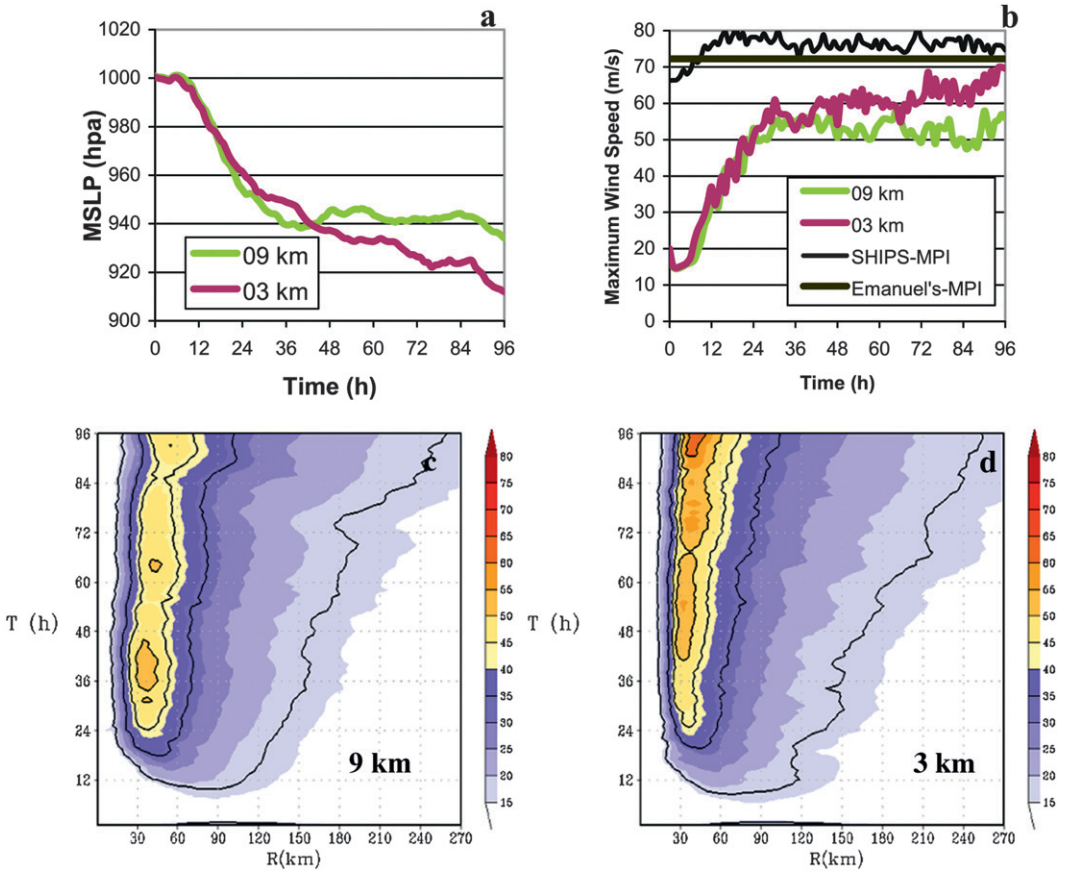

FIG. 2. Time history of the intensification process in an idealized storm for horizontal grid resolutions of 9 and 3 km: (a) MSLP in hPa, (b) maximum 10-m level wind speed in m s^{-1}, and Hovmöller diagrams of the axisymmetric mean tangential winds at a height of 10 m for the (c) 9- and (d) 3-km runs. The contour lines from the outer- to the inner-core regions are, respectively, 17.2, 33, 43, 50, and 59 m s^{-1}, representing the radius of gale-force winds and the core of hurricane winds starting from a minimal category 1 to a minimal category 4. The maximum potential intensity derived from SHIPS and Emanual's potential intensity theory is provided for reference in (b).

Du_r and Dv_λ are, respectively, the diffusion (frictional) terms in the radial and tangential directions. In the absence of friction and the forces that constitute balance, Eq. (1) reduces to the gradient wind equation (term A). Equation (2) represents the net forcing. Term B in Eq. (2) is known as the generalized Coriolis term, and its significance is discussed later in the text.

3. Results and discussion

a. Time series of the vortex developments

Figure 2 provides the time history of the intensification on the inner nests at 9- and 3-km resolution (C09 and C03, respectively). The maximum potential intensity in terms of the maximum 10-m wind derived from the Statistical Hurricane Intensity Prediction Scheme (SHIPS) and Emanual's potential intensity theory is also provided for reference. After an initial period of gestation where the "cold start" spinup of the modeled vortex takes place, a period of rapid intensification is observed starting at about 8 h in C09 and about 6 h in C03 and continuing almost up to 24–30 h. During this time, the mean sea level pressure (MSLP) is reduced by at least 60 hPa (Fig. 2a), and the maximum 10-m wind speed increases by 42 m s^{-1} in both cases (Fig. 2b). Such rapid deepening is not uncommon in Atlantic hurricanes (Kaplan et al. 2010). Further intensification is slow; however, significant differences can be seen in the deepening process between C09 and C03.

Figures 2c,d provide Hovmöller diagrams of the mean tangential winds at a height of 10 m for C09 and C03. The contour lines from the outer- to the inner-core regions are, respectively, 17.2, 33, 43, 50, and 59 m s^{-1}, depicting the radius of gale-force winds and the core of hurricane winds starting from a minimal category of 1 to a minimal category of 4. In general, the radius of

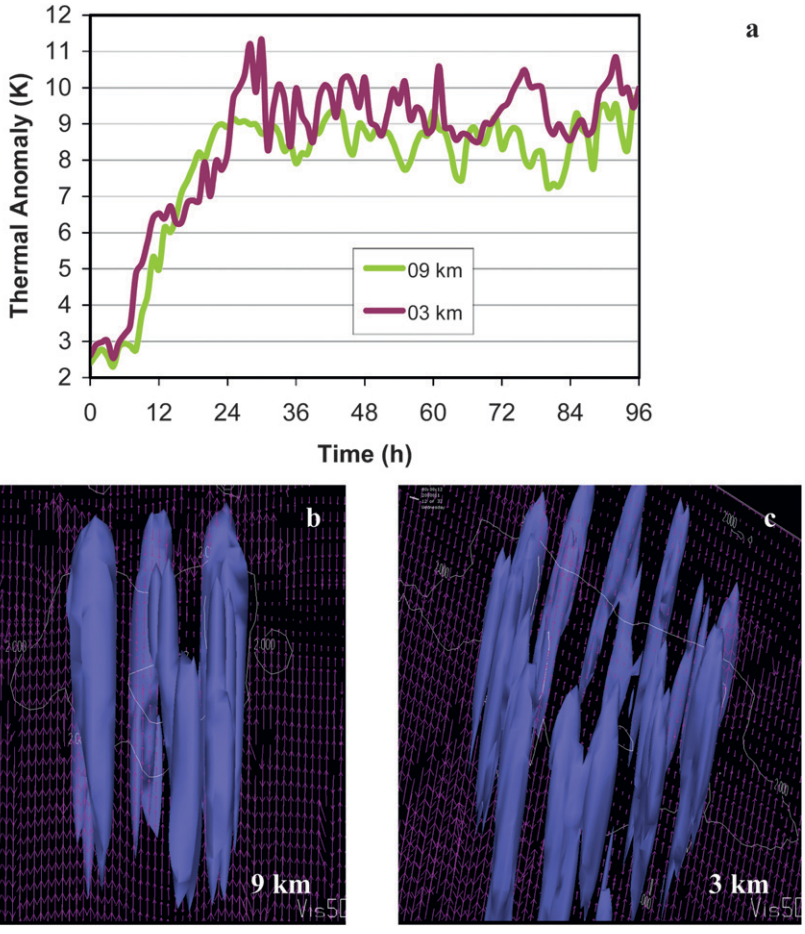

FIG. 3. Initial development. (a) The tangentially averaged maximum temperature anomaly (K) with respect to the far-field environmental temperature profile within the nested domain plotted hourly for the 9- and 3-km runs. Instantaneous plots of isosurfaces connecting the vertical velocity field of 2 m s^{-1} at (b) 9- and (c) 3-km resolutions. Figures 3b,c are only used to provide a qualitative description of the vertical acceleration of the thermal plumes discussed in the text.

maximum wind between 24 and 96 h is approximately 50 km, whereas the radius of gale-force wind keeps expanding during the same period of time. This is consistent with the known behavior of some of the intense Atlantic hurricanes (e.g., Hurricane Katrina, 2005; information online at http://www.nhc.noaa.gov/pdf/TCR-AL122005_Katrina.pdf). The inner core is consistently stronger in C03 than in C09, especially during the mature phase. A simulation of C03 attains a strength corresponding to category 4 at the end of the simulation, whereas C09 is barely a category 3 hurricane. Nevertheless, the evolution of the radius of the gale-force winds, which have a slower time scale (Smith et al. 2009) than the spinup of the inner core, is nearly identical in both runs. As shown later, it appears that the resolution within the eyewall region may be more important than having a uniformly large, very-high resolution nested domain in precisely forecasting the intensity changes in TCs.

b. *Rapid intensification stage: Warm-core development*

Central to the problem of intensification is the development of the warm core and the subsequent decrease in hydrostatic surface pressure. Figure 3 depicts various aspects of the warm-core development at 9- and 3-km resolutions (C09 and C03, respectively). As shown in Fig. 3a, the maximum tangentially averaged temperature anomaly within the nested domain is very well correlated[1] with the evolution of the MSLP (Fig. 2a).

[1] Although temperature may be hydrostatically related to pressure, θ_e, as advocated in Holland's maximum potential intensity theory (Holland 1997), it may be more accurately related to the pressure depressions in the eyes of TCs. However, for practical purposes (see Ritchie et al. 2003) and for ease of illustration, we simply correlate here the maximum temperature deviations in the warm-core region with pressure.

Nevertheless, to further understand the warm-core development from an initial temperature anomaly of about 2 K that was produced from the nonlinear balance method, we analyzed the three-dimensional evolution of instantaneous output obtained on the native rotated latitude–longitude system, but interpolated on the z-coordinate system at a 6-min interval between 0 and 24 h. During this time period, the MSLP decreased from about 1000 to 954 hPa (46 hPa in 24 h) for C09 and from about 1000 to 961 hPa (39 hPa in 24 h) for C03. The corresponding maximum tangentially averaged temperature anomaly was 8.9 K in C09 and 8.2 K in C03 (Fig. 3a).

The rapid warming of the core was closely associated with the development of organized moist, thermal plumes around the eyewall region. Figures 3b and 3c show an example of the 2-m s^{-1} vertical velocity isosurface in C09 and C03, respectively, during the start of the rapid intensification period. These ''organized plumes'' bear some analogy with the dry thermals in the boundary layer (Gopalakrishnan and Avissar 2000), but are moist, have a depth scale several times larger than those observed in the boundary layer, and are characterized by stronger vertical velocities in the mid- to upper troposphere. A qualitative comparison between C09 and C03 indicates that horizontal resolution has a pronounced impact on the structure of these plumes. The plumes occupy a larger area but are fewer in number for simulation C09 than in C03.

We examined the thermal anomaly associated with each of the plumes by differencing the instantaneous temperature at a given grid point with respect to the far-field environmental temperature profile within the nested domain. Although only a small part of this anomaly may be utilized for further warming of the existing warm core, such an analysis may be useful at least during the rapid intensification period where the thermal plume can be distinguished from the environment. Figures 4a,b for example, depict the x–z cross section of the instantaneous anomaly (color shaded) across an arbitrary plane in the eyewall region for C09 at about 9 h (Fig. 4a) and 24 h (Fig. 4b). The initial anomaly is 2 K and is also seen in the background. In this example, an average 6–9-K temperature anomaly is carried by individual updrafts with a vertical velocity of 4–5 m s^{-1} during the rapid intensification period that is consistent with the average warming in the mid- to upper troposphere (Fig. 3a). As depicted by the temperature anomaly and θ_e contours (indicated by black color), updrafts with a life cycle of about 15 min and an origin near the top of the boundary layer transport moisture and heat (higher θ_e air) into the upper troposphere (Emanuel 2003). In addition, heat is also added by cumulus convection. Willoughby (1979) showed that the radial gradient of convective heating alone is sufficient to create weak subsidence and radial motion (w and u_r). Consistent with Willoughby's findings, and aided by weak subsidence and by radial advection (not shown and the subject of future investigation), an initially weak warm core strengthens rapidly within the first 24 h (Figs. 3a and 4b,d). Finally, although the structure of the buoyant plumes may be different between C09 and C03 (Figs. 3c,d), interestingly, the intensification process was similar for this case (Table 1). At the end of the rapid intensification period, the maximum temperature anomaly was about 8–9 K, and the structure of the warm core exhibited major similarities (Figs. 4b,d). These estimates agree with those reported by Ritchie et al. (2003) for the case of Hurricane Floyd (1999).

c. *Asymmetries and extreme events*

A qualitative illustration of the warm-core development leading to rapid intensification of the TC vortex was provided above. While in a fully three-dimensional model it may not be possible to assess the influence of each of the thermal plumes on the intensification process, a statistical description may be useful. A simple diagnostic package was developed to find the mean, deviation, and maximum value of the extreme event associated with the plumes discussed in the previous section (Figs. 5a,b). Extreme events were determined by tracking the number of updrafts in the domain exceeding 5 m s^{-1}. The threshold value of 5 m s^{-1} is approximately the maximum standard deviation for the 3-km run (Fig. 5b). The thermal anomaly associated with these extreme events was also examined (Fig. 5c). Several features are worth noting:

- The tangentially averaged updrafts are characterized by a velocity of about 2 m s^{-1}, a range also consistent with simple axisymmetric models (Rotunno and Emanuel 1987). While the mean did not differ significantly between the C09 and C03 simulations, the latter simulation showed larger variance, especially during the rapid intensification period (Fig. 5a).
- The instantaneous maximum vertical velocity in C09 was about 22 m s^{-1} and as high as 48 m s^{-1} in C03 (Fig. 5a). However, at best, only 15% of the population of thermal plumes exceeded a speed of 5 m s^{-1} during the rapid intensification period in C03 (Fig. 5b). Interestingly, after the ninth hour where some extreme events were located in C09, these events became insignificant after 12 h (<5% of the population), indicating that the bulk of the moisture and heat from near the boundary layer were carried by thermal plumes with a tangentially averaged vertical velocity of 2 m s^{-1} (and a standard deviation of +2–3 m s^{-1} at

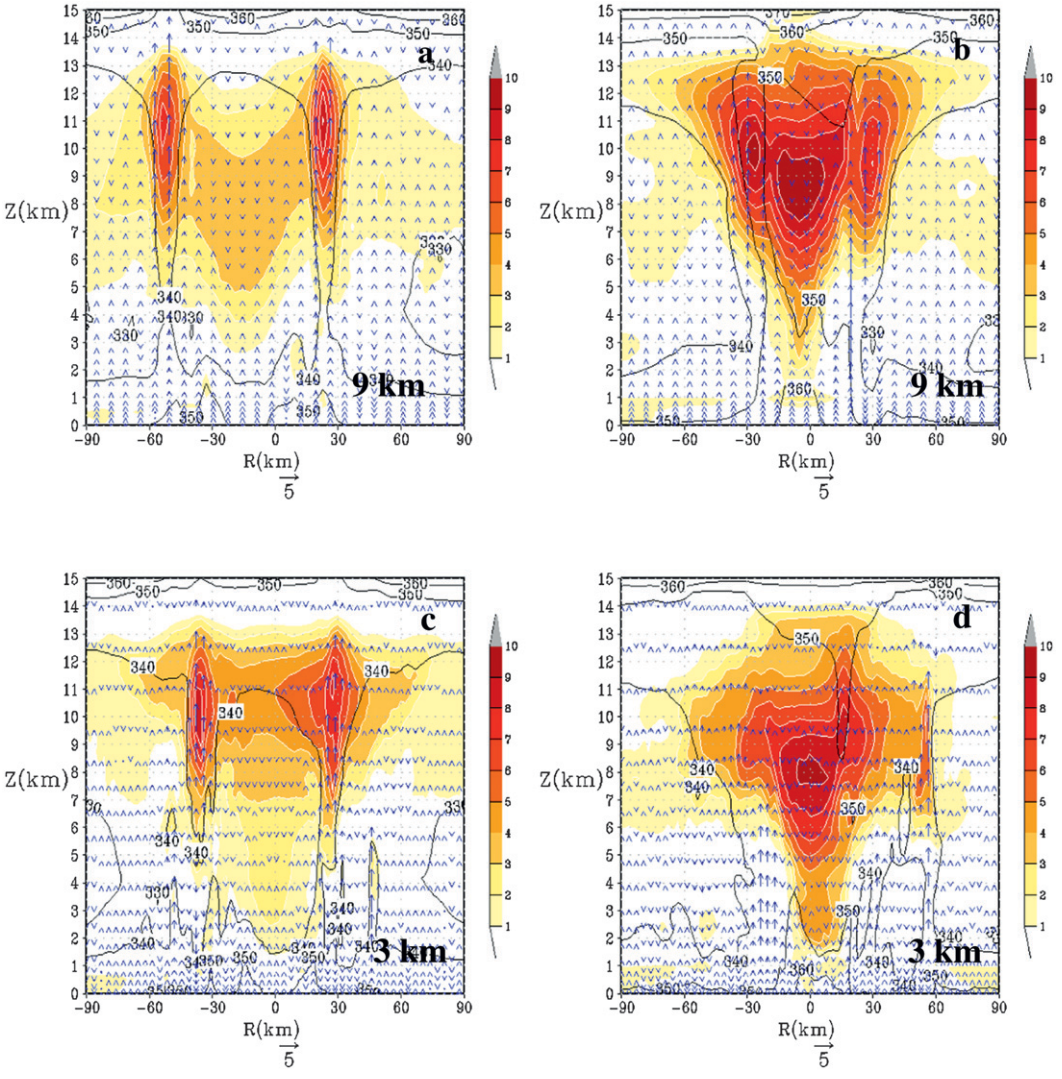

FIG. 4. Warm-core development. Depiction of the x–z cross section of the instantaneous temperature anomaly (color shaded) across an arbitrary plane in the eyewall region at about (a) 9 and (b) 24 h for the 9-km run. (c),(d) As in (a),(b), but for the 3-km run. The white contours are used to emphasize the nature of the thermal plumes within the warmer environment discussed in the text. As depicted by the temperature anomaly and θ_e (in K and contours indicated by black color), both moisture and heat are carried to the mid- and upper troposphere by the thermal plumes shown in Figs. 3b,c. The vector indicates the direction of the vertical motion. Although the model top extends to about 18 km, we have zoomed in on the region of interest, which for the description in this text is about 15 km.

about 10-km height). Except for the delay in the onset of intensification, most low-resolution models (Kurihara and Tuleya 1974), as well as axisymmetric models (e.g., Rotunno and Emanuel 1987), have been able to capture the rapid strengthening of an initially axisymmetric vortex consistent with the current framework.

- Recently, Rogers (2010) used MM5 model simulations at 1.67-km horizontal resolution from Hurricane Dennis and found that rapid intensity changes in TCs may not be tied to a dramatic increase in the number of convective bursts nor in the characteristics of the bursts, such as the burst intensity. The updrafts that represent the bulk of the vertical motion distributions rather than those at the extreme end of the spectrum contribute the most to the rapid intensification process. These results are also consistent with our current findings.
- Although the concept of buoyancy (Smith et al. 2005) is an issue of debate that we will explore in detail in a subsequent publication, it appears that some useful information about its thermal statistics may be extracted, at least during the initial phase of

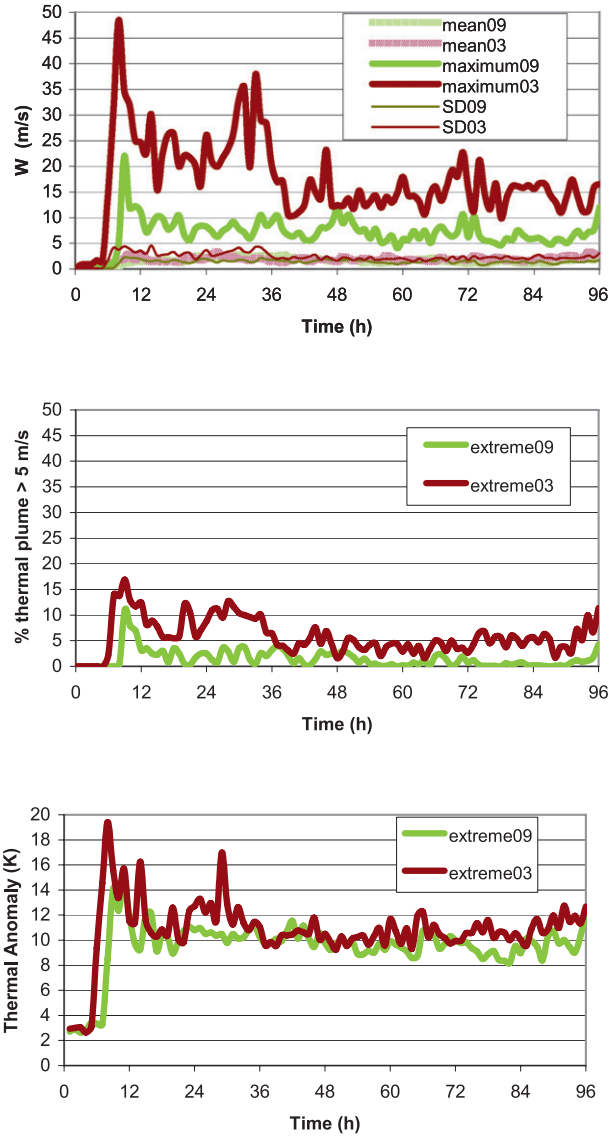

FIG. 5. Depiction of the updraft statistics for the 9- and 3-km runs for (a) the tangentially averaged maximum vertical velocity, standard deviation, and the maximum values, (b) the percentage of extreme events at a given time that is determined by vertical velocity exceeding 5 m s^{-1} to those between 0.5 and 5 m s^{-1} in a column, and (c) the thermal anomaly (K) corresponding to the maximum updraft velocity.

intensification when the thermal plumes can be distinctly identified even in the background of a warmer environment (Figs. 4a–d). Clearly, to produce the same type of warm core in C09 and C03 during the spinup process (Fig. 3a), these plumes should carry an equivalent amount of the thermal anomaly in either case. Evidently, the plumes with an average velocity of 2 m s^{-1}, which are approximately the same in C09 and C03 (Fig. 5a), should carry the bulk of the thermal anomaly to produce an equivalent warm core at either resolution. Additionally, as shown in Fig. 5c, extreme events carry a maximum of about 19 K for C03 during the initial spinup of the vortex. Interestingly, an updraft of 15–20 m s^{-1} in C09 also carries an equivalent amount of thermal anomaly (about 15 K).

d. Mature stage: Axisymmetric evolution

A finer horizontal model grid resolution (of 9 and 3 km) had minimum impact on the rapid intensification. However, the slower evolution of the mature storm (after about 2 days) is significantly influenced by resolution (Figs. 2a,b and 3a). As will become evident in this section, axisymmetric reasoning can be used to explain the slow evolution of the storm in 9- and 3-km runs (C09 and C03, respectively). We made an hourly analysis of the mean structure of the storm for 93 h starting at hour 3. However, for the sake of brevity we only present the salient features of that analysis here.

Figure 6, for instance, shows the tangentially averaged, 6-hourly time-averaged, radius–height cross section of the secondary circulation at 21 and 93 h, respectively, representing the mean structure near the end of the rapid intensification period and mature storm stage for C09 and C03. As indicated by the vectors and contours in Fig. 6, the circulation is characterized by a deep layer of radial inflow almost a couple of kilometers deep in the lower troposphere and a layer of intense outflow (shown in dotted contours) characterizing the upper-level divergence at about 14-km height. The rising branch of the secondary circulation, depicted in color shading and located in the eyewall region, slopes radially outward. A weak outflow is observed above the shallow inflow layer due to the return flow and becomes more evident as the storm intensifies (Figs. 6b,d). The model is able to reproduce some of the observed axisymmetric features of the secondary circulation that are well documented in Marks and Houze (1987). Of specific significance to the intensification problem is the weak inflow in the mid- to upper troposphere. Several axisymmetric model studies (e.g., Ooyama 1982; Willoughby 1979; Yamasaki 1977) have illustrated the importance of this inflow layer to the slow evolution of a TC vortex. Ooyama (1982) pointed out that the deep-layer inflow is, in essence, all that is needed for intensification of cyclonic rotation because at that level surface friction may not affect the evolution process. Willoughby (1979) pointed out that the development of this weak inflow may be related to inner-core warming. Minor differences between C09 and C03 may be linked to a stronger thermal anomaly in C03 than in C09 (Fig. 3a). Additionally, as illustrated in Figs. 6a,c the

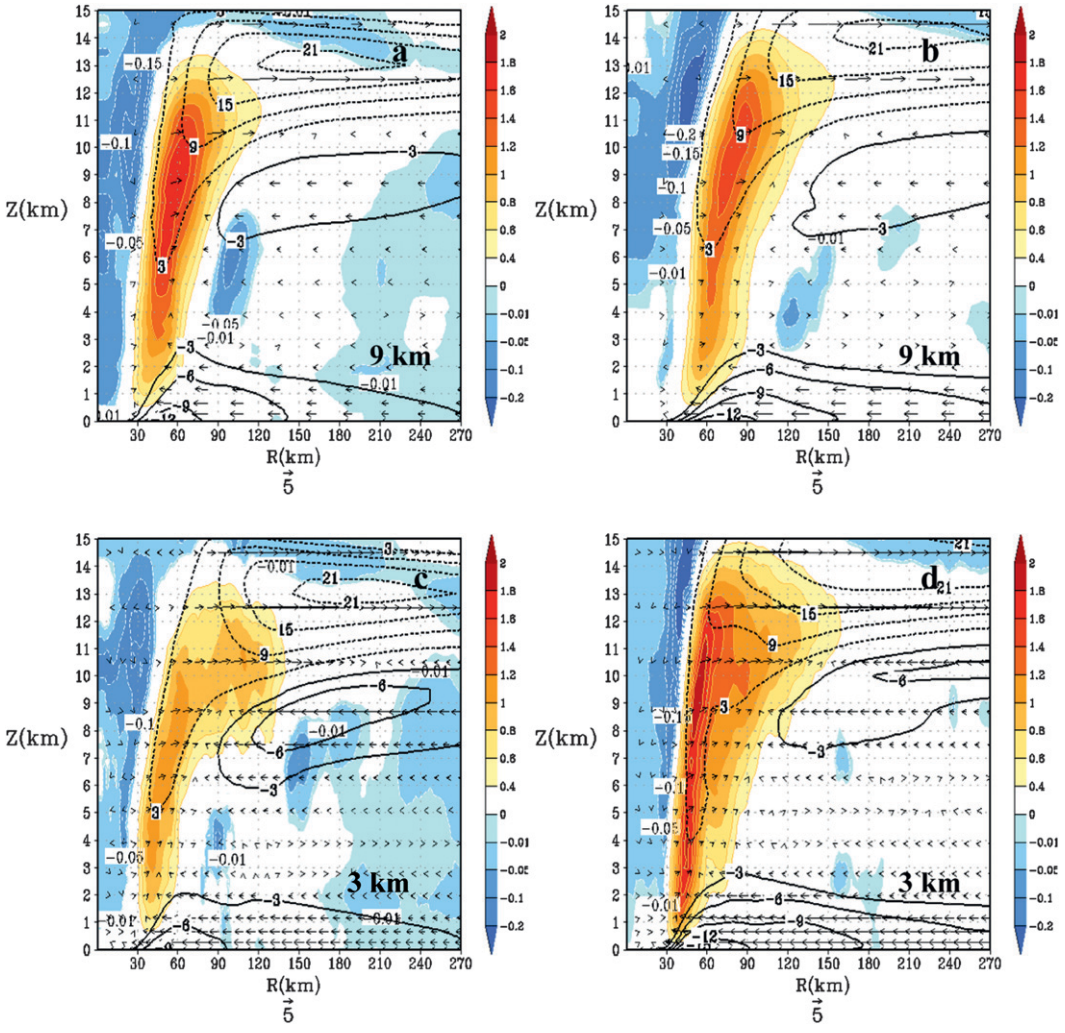

FIG. 6. The tangentially averaged, 6-hourly time-averaged, radius–height cross section of the secondary circulation at 21 and 93 h for the (a),(b) 9- and (c),(d) 3-km runs. The black solid contour indicates the inflow, and the dotted contours show the outflow of the radial wind component (m s^{-1}). The vertical velocity (m s^{-1}) is shaded with positive upward motion, as indicated by the red end of the spectrum and with weak subsidence indicated by the blue end of the spectrum. Because the distribution of the vertical velocity is skewed, please note that the scales are unequally spaced. For convenience, the vector field obtained that compounded the tangentially averaged vertical and the radial velocity components is also provided here. Although the model top extends to about 18 km, we have zoomed in on the region of interest, which for the description in this text is about 15 km.

secondary circulation is well established even around 21 h in either case (C09 and C03), and the radial inflow intensifies with time. The secondary circulation is characterized by more organized updrafts that have an average velocity of 2–3 m s^{-1} in the eyewall region (red color shades) and weak subsidence in the central core (blue shades in Figs. 6a–d). Although there is no accepted theory at this time to explain the formation and maintenance of a hurricane eye, as in the case of an evolving storm, radial gradients in convective heating that are primarily driven by the updrafts in the eyewall region may be associated with the formation of the eye (Willoughby 1979). Significant subsidence is observed close to the inner edge of the eyewall. This pronounced subsidence near the eyewall is supported by observations (e.g., Jorgensen 1984; Marks et al. 1992). Interestingly, very small differences are observed in the strength of the mean secondary circulation between C09 and C03, a fact that will be emphasized later in this section as well.

Figure 7 depicts the tangentially averaged, 6-hourly time-averaged, radius–height cross section of the net radial force in the governing equation for the secondary circulation *without including frictional effects* [i.e., term

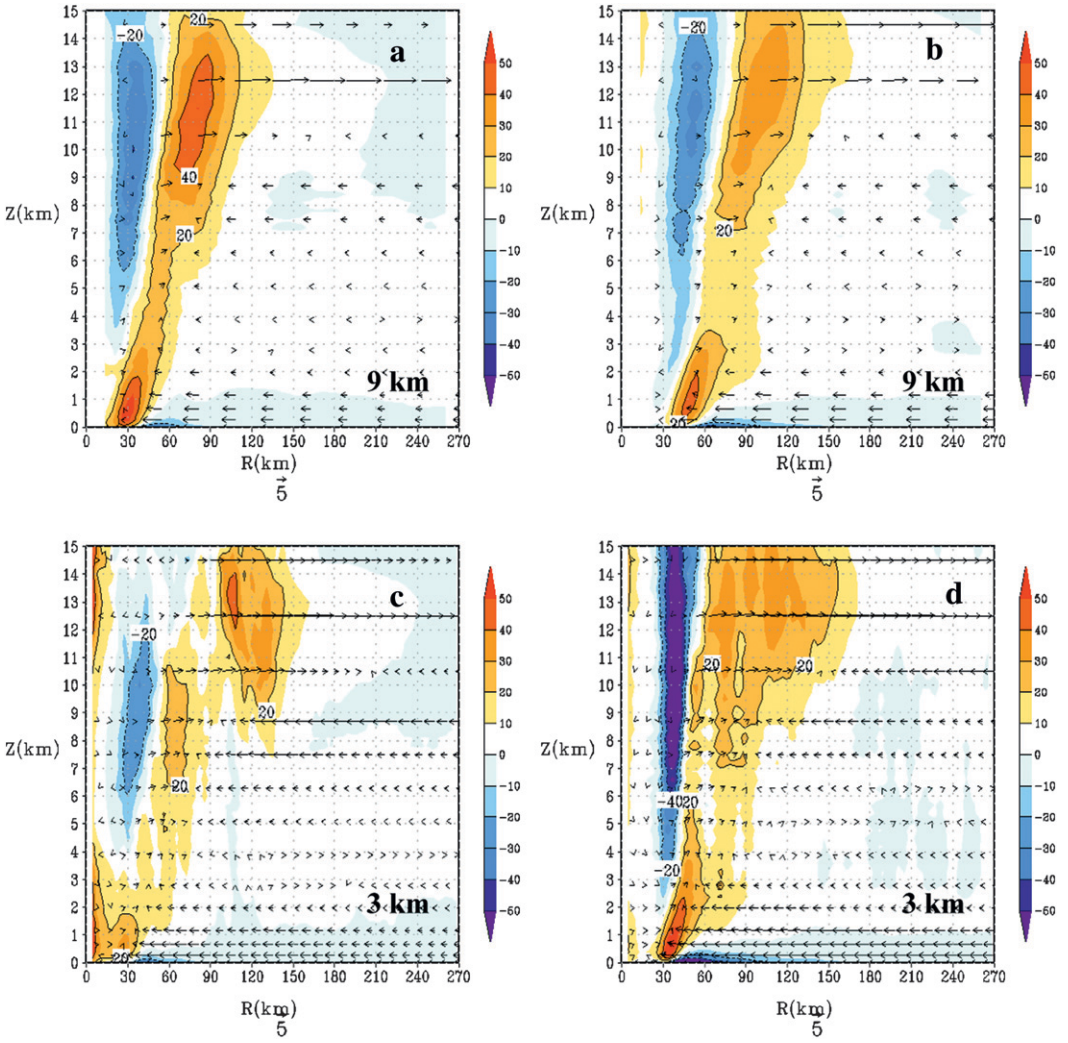

FIG. 7. Depiction of the tangentially averaged, 6-hourly time-averaged, radius–height cross section of the net radial force (m s^{-1} h^{-1}), excluding frictional effects [term A in Eq. (1)] at (left) 21 and (right) 93 h, for the (a),(b) 9- and (c),(d) 3-km runs. The red end of the spectrum indicates the supergradient and blue end of the spectrum indicates subgradients.

A in Eq. (1)] at 21 and 93 h for C09 and C03. Several features are worth noting:

- Starting with the earliest work on the evolution of a balanced vortex by Eliassen (1951), several theoretical models have assumed that the acceleration and frictional terms in Eq. (1) that describe the secondary circulation may be neglected so that the vortex is in a state of gradient wind balance (e.g., Emanuel 1986; Willoughby 1990a,b; Willoughby 2009; Pendergrass and Willoughby 2009). Willoughby (1990b) used numerous aircraft observations and found that such an approximation was indeed valid and useful in describing the tangentially averaged tangential wind above the boundary layer (Zhang et al. 2001). Clearly, a gradient wind balance prevails at least in the region of weak inflow (indicated by 3–6 m s^{-1} contour lines between 8 and 9 km in Fig. 6) above the atmospheric boundary layer (ABL).
- In general, the ABL and eyewall region are characterized by very strong imbalances of the gradient wind. Additionally, some imbalance prevails in the region of the outflow.
- Within the ABL, winds are subgradient in the outer radii but become supergradient in the eyewall region where the inflow diminishes in magnitude and the convective updraft erupts. Zhang et al. (2001) and Smith et al. (2009) attributed the inner-core spinup to the existence of the unbalanced flows. Specifically, the supergradient tangential winds in the region of decelerating inflow are carried upward and outward to feed into the eyewall cloud. Our studies also show the

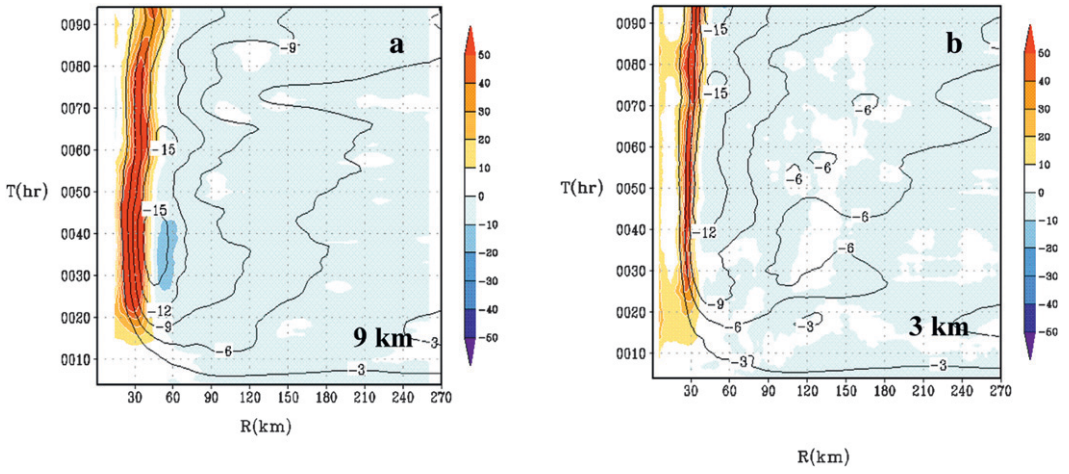

FIG. 8. Hovmöller diagram of the tangentially averaged, 6-hourly time-averaged net radial forcing term (m s^{-1} h^{-1}) in the governing equation for the secondary circulation with friction (i.e., sum of the pressure gradient, Coriolis, centripetal, and frictional forces) for the (a) 9- and (b) 3-km runs at the 30-m level. The blue end of the spectrum represents the radial acceleration, and the red end of the spectrum represents the deceleration. Superposed on color shades are the contours of the radial component of the velocity (m s^{-1}).

presence of supergradient wind both for C09 and C03 (Fig. 7).

- It is not clear at this time what the impacts may be of the imbalance in the statically stable region of the outflow. However, imbalance in the inner edge of the eyewall region may be a result of adverse axial pressure gradients (Smith 1980). The maximum tangential wind tilts and decreases with height, whereas the pressure gradient force [in Eq. (1)] has an upright distribution (not shown). The net effect leads to the pressure gradient force acting inward (from the eyewall to the eye). Nevertheless, Smith (1980) found that the buoyancy force due to adiabatic warming almost exactly counteracted this pressure gradient. The stronger subsidence close to the eyewall in the mid- to upper troposphere in Fig. 6 is consistent with the above argument.
- At about 21 h, C09 illustrates a more evolved structure than C03 (Figs. 6a,c). Nevertheless, there are no significant differences in the structure of the agradient forcing term in a mature storm (Figs. 7b,d), nor could we notice any significant effects of resolution in either case (Figs. 7a–d).
- Figure 8 provides a Hovmöller diagram of the tangentially averaged, 6-hourly time-averaged net radial forcing term in the governing equation for the secondary circulation *with friction* (i.e., the sum of the pressure gradient, Coriolis, centrifugal, and frictional forces) for the 9- and 3-km runs at the 30-m level. The blue end of the spectrum represents radial acceleration, and the red end of the spectrum represents deceleration. Superposed on the colored shades are the contours of the radial component of velocity (in m s^{-1}). Clearly, although the supergradient wind appears to be broader in C09, resolution has very little impact on the intensity of the secondary circulation (i.e., on the radial component of the velocity) near the surface. Additionally, the contributions from the imbalances (subgradient flow) are diminished due to friction for both C09 and C03.

Figure 9 depicts the tangentially averaged, 6-hourly time-averaged radius–height cross section of the tangential wind contours superposed net forcing in the tangential direction [i.e., Eq. (2)] at 21, 45, and 93 h for C09 and C03. It should be emphasized that the frictional terms were included in this computation. Several features are worth noting:

- The maximum tangential wind speed occurs within the inflow layer and, following the contours for gale-force wind (black contours between 15 and 20 m s^{-1}), the circulation expands with time for both C09 and C03, consistent with the behavior of the near-surface winds (Figs. 2c,d). Interestingly, the maximum wind contour is observed to be located between 30 and 50 km for both C09 and C03 (Figs. 9a–f). However, the tilt of the maximum wind with height is observed to be larger for C09 than for C03 at both 45 and 93 h, indicating a tighter and deeper vortex in C03. This is again consistent with Figs. 2c,d and with Fierro et al. (2009). Nevertheless, it appears that the differences are more or less restricted to the inner core. For instance, during 90–96 h, the maximum tangential wind for C09 in the inner core is about 60 m s^{-1}, whereas it is about

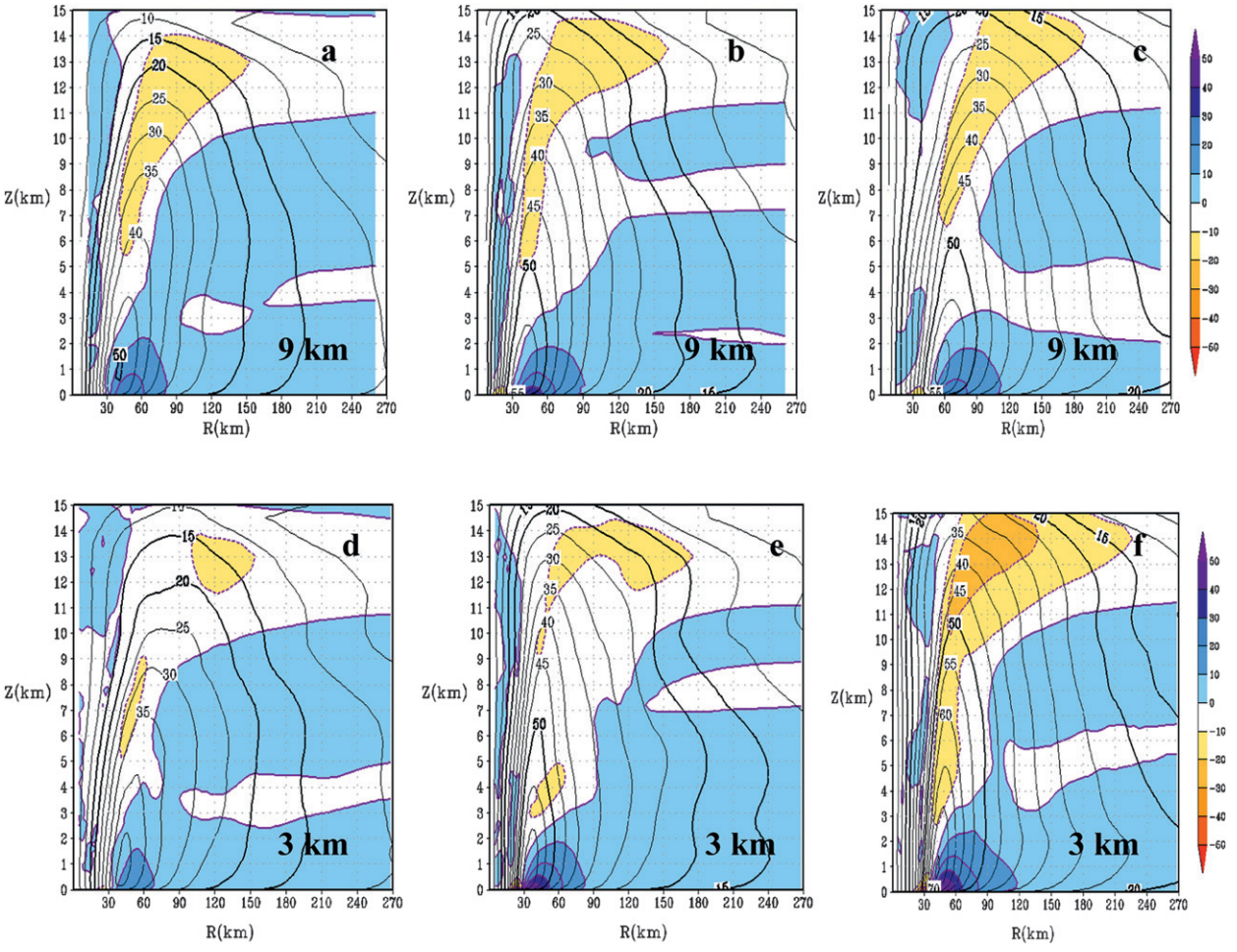

FIG. 9. Depiction of the tangentially averaged, 6-hourly time-averaged, radius–height cross section of the tangential wind contours (in red) superposed on top of the net tangential forcing (*frictional effect included*) (m s^{-1} h^{-1}, color shaded) related to the primary circulation term in Eq. (2) at (left) 21, (middle) 45, and (right) 93 h for the (a)–(c) 9- and (d)–(f) 3-km runs. In general, the positive contribution toward the spinup process is indicated by the blue end of the spectrum. It should be emphasized that the frictional terms were included in this computation. The radius of gale-force wind (between 15 and 20 m s^{-1}) and the 50 m s^{-1} contours are depicted in black.

75 m s^{-1} in C03. However, at a radius of 210 km, the strength of the wind varies between 15 and 20 m s^{-1} up to about 12-km altitude in either case.

- The weak inflow above the boundary layer contributes to the net intensification process. However, the strongest forcing that results in tangential acceleration and spinup of the vortex is seen to occur near the surface despite the effects of friction, which acts in the tangential direction. Clearly, in both cases the positive contribution toward the vortex spinup grows with time. However, the near-surface contribution for C03 is stronger at 45 and 93 h (Figs. 9e,f) when compared to C09 (Figs. 9b,c).
- Currently, intensity-forecasting models for TCs show a great deal of sensitivity to their boundary layer parameterization schemes. Considering the above results, which illustrate the importance of convergence around the eyewall boundary layers in TCs, it is not surprising that different boundary layer parameterization schemes in models produce different results for intensity forecasting (see, e.g., Braun and Tao 2000). A careful reevaluation of the boundary layer processes and the agradient terms within the context of the ideal vortex is important and will be a part of our follow-up study (J.-W. Bao 2010, personal communication).

To isolate the major contribution to the tangential acceleration in the boundary layer, we examined the individual terms in Eq. (2). Figures 10a,b show the Hovmöller plot of the tangentially averaged, time-averaged generalized Coriolis term *including the effects of a frictional term* at the 30-m level for both C09 and

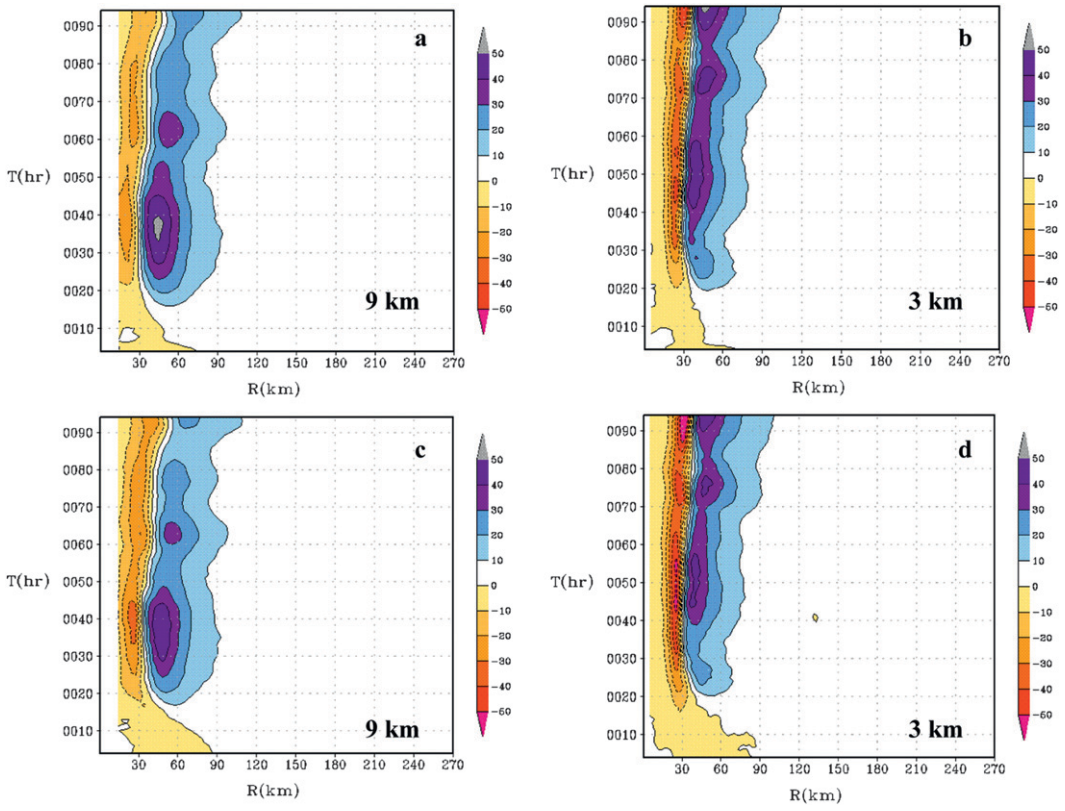

FIG. 10. (a),(b) Hovmöller plot of a tangentially averaged, 6-hourly time-averaged generalized Coriolis term *with the addition of a frictional effect* at the 30-m level for the (a) 9- and (b) 3-km runs and the radial advection of tangential wind for the (c) 9- and (d) 3-km runs. Units are m s^{-1} h^{-1}.

C03. In either case, the spinup process was restricted to the inner-core region. However, significant differences in the evolution of the inner core can be observed between C09 and C03. C03 is consistently stronger than C09, leading to stronger winds in the inner core as shown in Figs. 2c,d. Although the secondary circulation near the surface (Figs. 8a,b) showed little sensitivity to resolution, the coupled term (term B) in Eq. (2) showed more sensitivity, especially in the mature phase of the storm (24–96 h). Further examination of the local tendency budget term shows that the radial advection of tangential wind exhibited a significant difference in evolution between C09 and C03 (Figs. 10c,d). Although the radial velocity evolution is insensitive to resolution, the tangential gradients are better resolved with finer resolution. In other words, intensification in TCs occurs by means of cooperative interaction between the primary and the secondary circulations. The radial flux of absolute vorticity, which is the sum of the generalized Coriolis term and the radial advection of tangential velocity, becomes an important forcing term in the momentum budget equations for the mature storm [Eqs. (1) and (2)].

Figure 11 provides an overview of the thermodynamic structure at 69 and 93 h for C09 and C03. These hours were chosen as an indictor for the analysis of a mature storm. Nevertheless, the results can be generalized. The tangentially averaged, 6-hourly time-averaged, radius–height cross section of θ_e and the advected moisture fluxes are provided here. The mean θ_e is illustrated in shaded colors, and the moisture fluxes are indicated by blue-colored contour lines. Several features in this figure are noteworthy:

- The mean θ_e cross section exhibits classic characteristics of a warm-core system that is well supported by observations and documented in several works (e.g., Hawkins and Imbembo 1976).
- Eyewall convection is the main agent transferring higher-θ_e air from the ocean surface to the upper troposphere (see Plate 1b in Emanuel 2003, for a classic view of this transport). The radial gradient of θ_e during the initial stage of the storm initiates subsidence (Figs. 4a,c). Subsidence is enhanced with the formation of a well-defined eye and this, in turn, leads to a strengthening of the storm at a subsequent time

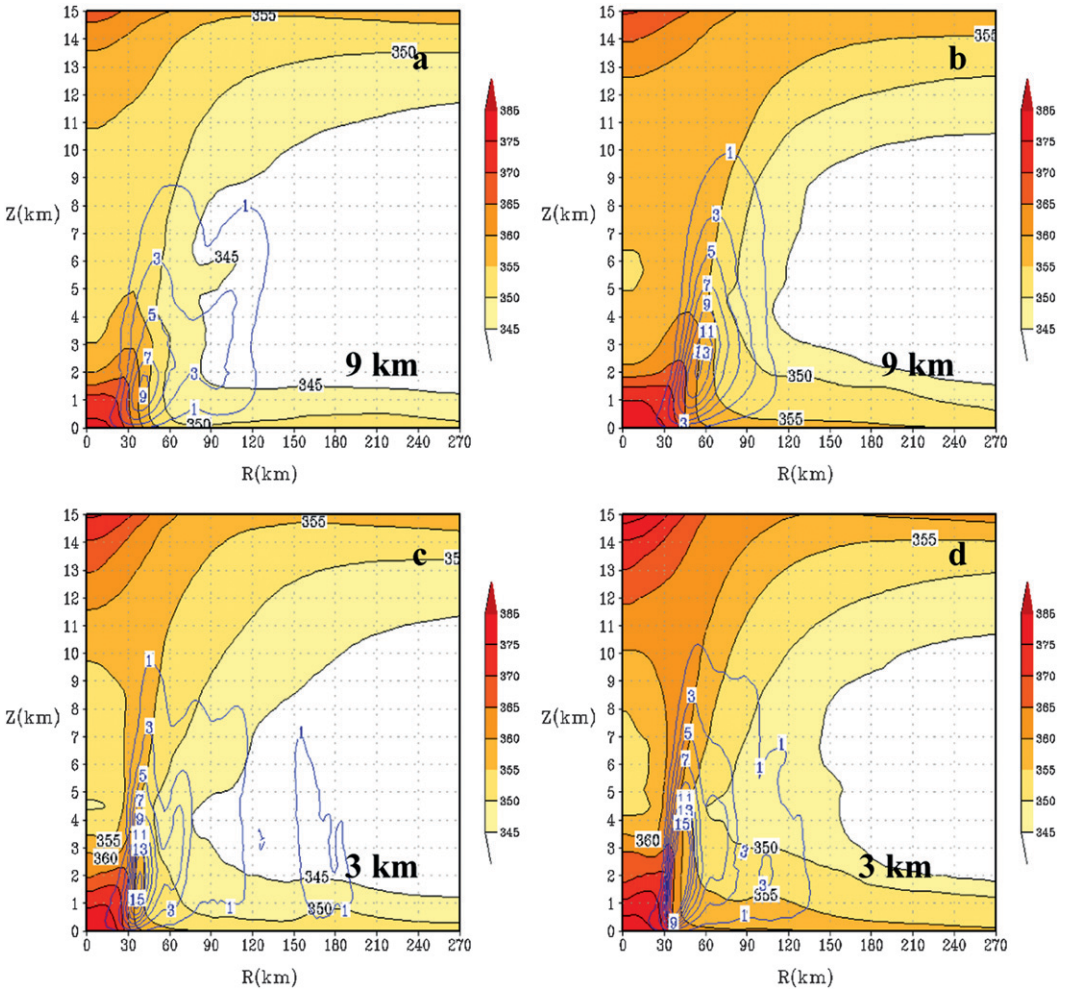

FIG. 11. An overview of the thermodynamic structure in a mature storm around 69 and 93 h for the (a),(b) 9- and (c),(d) 3-km runs. The tangentially averaged, 6-hourly time-averaged, radius–height cross section of θ_e and moisture fluxes are provided here. The mean θ_e is illustrated in shaded colors, and moisture fluxes are indicated by blue contour lines.

(e.g., Figs. 6b,d). The warmer the core, the larger the pressure drops at the surface. Malkus and Riehl (1960) illustrated that the θ_e anomaly is proportional to the pressure deficit at the center of the storm. They found that the proportionality constant may be on the order of 2.5. The warm cores in C09, as well as in C03, are consistent with the central pressure in either case. Additionally, the mean θ_e in the eyewall for C09 at 69 h is about 350 K; it increases to 355 K at 93 h for the same run. However, for C03 it is 355 K at 69 h and 360 K at 93 h. Clearly, C03 has a warmer core than C09 and, consequently, there is at least a 20-hPa pressure difference between C09 and C03 in the case of a mature storm.

- The process of intensification occurs through the feedback between the mass and wind fields. The warmer the core (Fig. 11c), the deeper the pressure (Fig. 2a) and the stronger the wind at the surface (Fig. 2b). Finer resolution in the eyewall region not only produces stronger convergence, stronger tangential winds near the surface (Figs. 9e,f), and larger ocean fluxes (not shown), but also provides higher and better-defined moisture flux gradients above the air–sea layer. This can be illustrated by a comparison between C09 and C03 in terms of moisture fluxes (Figs. 11a–d). The moisture fluxes are not only higher for C03 but also the radial gradients of these fluxes are sharper along the eyewall edge as in a frontal boundary (Emanuel 1997). This leads to transport of higher-θ_e air and the subsequent intensification process continues.

4. Sensitivity experiments

In this section, we performed a few sensitivity experiments to seek answers to the following questions: (i) What is the model sensitivity to an initially stronger storm? (ii) How does the model respond to an initially bigger storm? (iii) What is the sensitivity of the above results to convective parameterization at 9- and-3 km resolution? Sensitivity experiments related to surface, boundary layer, microphysical, and radiation parameterization schemes will be reported upon in a complementary paper.

Figure 12 depicts the impacts of the initial strength of the vortex (Table 1). Figure 12a provides the time history of the intensification on the inner nests at 9- and 3-km resolutions (S09 and S03, respectively). Clearly, a stronger initial vortex produces a uniformly stronger storm. The storm in S03, for instance, reaches the potential intensity more rapidly than in C03. A comparison between C09 (Fig. 2c) and S09 (Fig. 12b) indicates that the inner core of the mature storm is much stronger in S09 than in C09. The strength of the inner core in S03 (Fig. 12c) also shows a corresponding increase when compared to C03 (Fig. 2d). In general, the size of the storm is bigger than those observed in the control simulations. Nevertheless, as indicated by the maximum 10-m wind (Fig. 12a), although the rapid intensification phase is uninfluenced by resolution, the mature storm in S03 is stronger than in S09, consistent with our earlier results.

Figure 13 illustrates the importance of the initial radius of the maximum wind. Figure 13a provides the time history of the intensification on the inner nests at 9- and 3-km resolutions (R09 and R03, respectively). Clearly, an initially larger storm of radius 120 km is as well resolved with a horizontal grid spacing of 9 km as those with a horizontal grid spacing of 3 km. The core heating in either case is nearly the same (Fig. 13a). Subsequently, the storm evolution, as depicted by the 10-m winds in R09 and R03, is comparable (Figs. 13b,c). For this case, we also examined the extreme event statistics similar to those discussed in section 3c. Interestingly, the ratio of extreme events determined by a vertical velocity exceeding 5 m s^{-1} to those between 0.5 and 5 m s^{-1} in a column in R03 was consistently higher than for R09 during 1–96 h of simulation. Nevertheless, both of the runs intensified to the same strength, indicating that the asymmetries related to extreme events had little influence on the growth of the storm (Figs. 13b,c).

Figure 14 illustrates the importance of convective parameterization within the nested domain at 9- and 3-km resolutions (Table 1; SAS09 and SAS03). The SAS

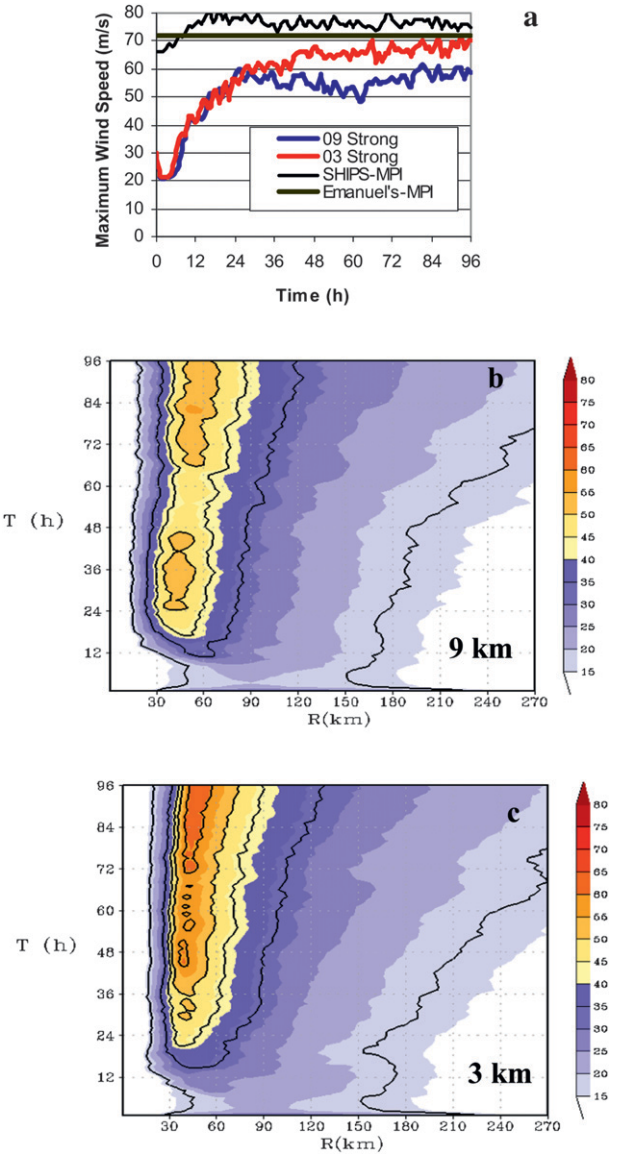

FIG. 12. Sensitivity experiments with the initial conditions for a stronger vortex starting at about 30 m s^{-1}: (a) maximum 10-m-level wind speed in m s^{-1}, and Hovmöller diagrams of the mean tangential winds for the (b) 9- and (c) 3-km runs. The maximum potential intensity derived from SHIPS and Emanual's potential intensity theory is provided for reference in (a).

convection scheme was switched off for the nested domain for SAS03 and SAS09. The tangentially averaged maximum temperature anomaly (K) with respect to the far-field environmental temperature profile within the nested domain is plotted hourly for these runs in Fig. 14a. The Hovmöller diagrams of the mean tangential winds for the SAS09 simulation (Fig. 14b) and the SAS03 simulation (Fig. 14c) are also shown. A comparison between Figs. 3a and 14a indicates that the resolvable-scale microphysical heating is too weak to

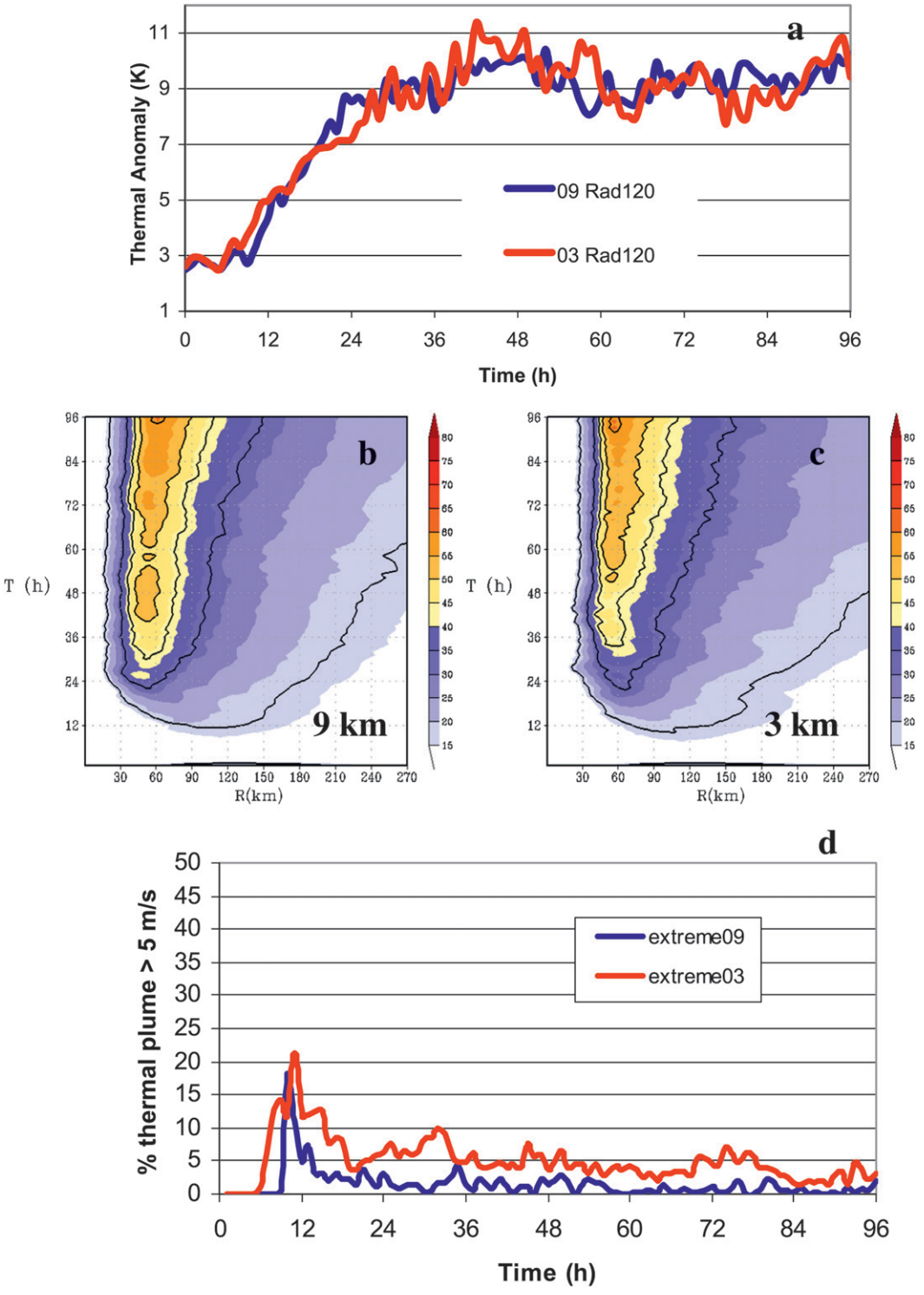

FIG. 13. Sensitivity experiments with the initial conditions for a larger vortex starting at about 120 km. (a) The tangentially averaged maximum temperature anomaly (K) with respect to the far-field environmental temperature profile within the nested domain plotted hourly for the 9- and 3-km runs, and Hovmöller diagrams of the mean tangential winds for the (b) 9- and (c) 3-km runs. (d) The ratio of extreme events determined by vertical velocity exceeding 5 m s^{-1} to those less than 5 m s^{-1} in a column.

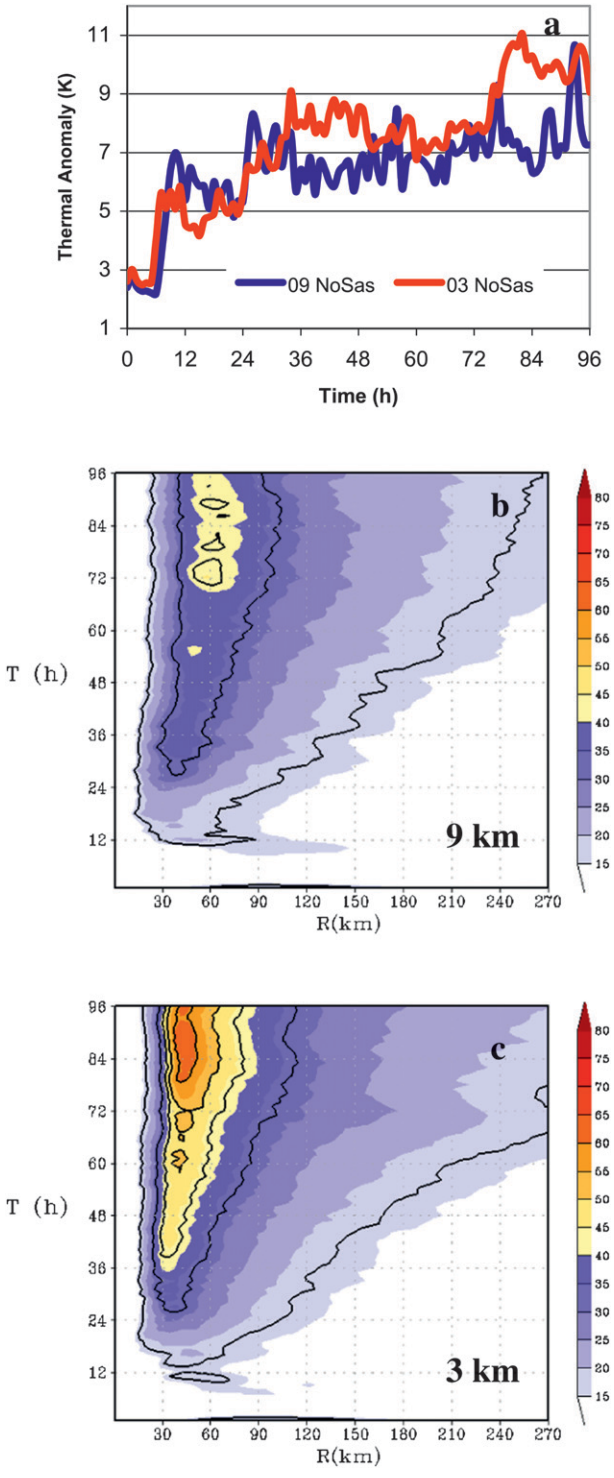

FIG. 14. Sensitivity experiments with the cumulus parameterization scheme, with the SAS convection scheme switched off for the nested domain at 9- and 3-km resolutions. (a) The tangentially averaged maximum temperature anomaly (K) with respect to the far-field environmental temperature profile within the nested domain plotted hourly for the 9- and 3-km runs, and Hovmöller diagrams of the mean tangential winds for the (b) 9- and (c) 3-km runs.

sustain a strong storm for the SAS09 simulation. Interestingly, for the C03 simulation, it appears that SAS convection provides additional heating, even at 3-km resolution for the rapid intensification event (Fig. 3a). However, by switching off this additional heating the rapid intensification phase is significantly modified in SAS03 (Fig. 14a). Nevertheless, the storm slowly intensifies to category 4 status (Fig. 14c). To obtain the same rapid intensification as C03, it appears that, for the current microphysics parameterization used in the model, the SAS convection scheme may not be neglected, even at the 3-km resolution.

5. Conclusions

Although significant improvements in hurricane track forecasting with numerical models have been made in the last decade, intensity forecasts need to be improved substantially. NOAA's Hurricane Forecast Improvement project (HFIP) is the next-generation effort in this direction. The first step toward this effort is to quantify the impacts of increased horizontal resolution in numerical models on intensity forecast. HFIP established in early 2009 the high resolution hurricane (HRH) tests. The plan for these tests was developed jointly by several segments of the community including specialists in hurricanes, numerical modeling, and forecast verification. The goal of the HRH tests was to evaluate the performance of various research models on a total of 69 forecast cycles of selected storms from the 2005 and 2007 seasons (for more details, please refer to the following Web site: http://www.dtcenter.org/plots/hrh_test/HRH_Report_30Sept.pdf). HWRFX participated in HFIP's HRH tests and the performance of HWRFX for these test cases is described in Zhang et al. (2011). Nevertheless, none of the cases included an idealized suite of tests that we believe is very important for understanding the intensity change problem. In this paper, we seek a basic understanding of the intensification process of an initially cloud-free, axisymmetric, baroclinic vortex on an f plane in a shear-free environment over a warm ocean with fixed sea surface temperatures in a weak easterly current of 4 m s^{-1} (ideal vortex, henceforth) using the HWRFX system. Specifically, we looked at three issues: (i) Does the new forecasting system produce the fundamental features of vortex spinup consistent with some of the observations and theoretical works? (ii) What is the role of convective asymmetries on the initial intensification of the storm? (iii) What are the impacts of model grid resolution on the evolution of the TCs? We believe that the third aspect of this problem may be useful to the forecasting community as well. HWRFX was run for 96 h (4 days) with two kinds of

horizontal resolution, namely, (i) a parent domain at a resolution of about 27 km with a 9-km moving nest and (ii) a parent domain at a resolution of 9 km with a moving nest at 3 km. While the former was more consistent with the current operational resolution, the latter could be the possible choice in the future. From our studies it appears that the following conclusions may be drawn:

1) The HWRFX produces vortex intensification consistent with other theoretical and numerical studies. After an initial period of gestation that lasts for about 6 h, the intensification of the vortex may be classified into a rapid intensification period (between 6 and 36 h) and a mature phase where the evolution is slow (i.e., between 36 and 96 h).
2) Buoyant updrafts appear to play a major role in the rapid intensification process. Thermal, moist plumes that have their origin in the ABL transport moisture and heat into the upper troposphere. Nguyen et al. (2008) provide evidence of cyclonic rotation of updrafts and eventual aggregation of these updrafts during the formation of the warm core. Aided by subsidence and, very likely, by radial advection, an initially weak warm core strengthens rapidly. Although the structure of the buoyant plumes may be different at 9- and 3-km resolutions, it appears that organized updrafts with a tangentially averaged velocity of about 2 m s^{-1} (with a standard deviation of +2–3 m s^{-1}) rather than the those at the extreme end of the spectrum may be responsible for providing the core warming, a consequent decrease in the hydrostatic surface pressure, and a subsequent increase in the surface winds that result in a further increase in the ocean fluxes.
3) Convective asymmetries as quantified by extreme events here are significantly influenced by resolution. The high-resolution simulation at 3 km produced updrafts as large as 48 m s^{-1}, whereas at 9-km resolution the maximum did not exceed about 22 m s^{-1}. However, the corresponding thermal anomaly did not scale accordingly (a 48 m s^{-1} updraft was warmer than the environment by 19 K, whereas a 22 m s^{-1} updraft was warmer than the environment by about 15 K). Additionally, the rapid spinup of the vortex at 3-km resolution was dominated by extreme events, whereas larger (in terms of areal coverage) and less intense updrafts were observed in the 9-km run during the same period of time. Nevertheless, interestingly, the 3- and 9-km-simulations produced a warm core of equivalent strength at the end of the rapid intensification period indicating that, at least for an initially axisymmetric vortex, the initial spinup in the models may not be critically dependent on these extreme events.
4) Although resolution had minimum impacts on the rapid intensification of an idealized TC, significant deviations were observed in the subsequent evolution of the storm. For instance, while the minimum pressure at the end of 96 h was 934 hPa for the 9-km simulation, it was about 910 hPa for the 3-km run. The axisymmetric budgets of radial and tangential momentum reveal that the evolution of a mature TC occurs through cooperative interaction between the primary and secondary circulation patterns. Radial advection of angular momentum within the boundary layer is an important forcing term in the dynamical budget and is dependent on the model grid resolution. Stronger convergence in the boundary layer leads to the improved transport of moisture fluxes and, subsequently, a stronger storm at higher resolution.

The above set of conclusions is based on the evolution of an initially axisymmetric vortex on an *f* plane in a shear-free environment over a warm ocean with fixed sea surface temperatures. Kaplan and DeMaria (2003) and Kaplan et al. (2010), using the SHIPS database, identified several environmental and vortex conditions that could especially affect the rapid intensification of the TCs. The impacts of shear, the spatial variations in SSTs and tropospheric relative humidity, the dynamics of the upper atmosphere (e.g., upper level divergence), and initial convective asymmetries all make the intensity problem challenging. The findings of Kaplan and DeMaria indicate that almost 35% of the intensity variance related to intensity changes in TCs may be attributed to environmental factors. Interestingly, the authors also find that an initially symmetric vortex has more chances to rapidly intensify (Kaplan et al. 2010). Additionally, in the recent literature several simulations of model sensitivities especially related to the parameterization of boundary layer processes and microphysical schemes have been reported. For instance, using a triply nested movable mesh, the Tropical Cyclone Model (TCM) developed at the University of Hawaii (Wang 2002a–c, 2009) has provided several insights into the impacts of cloud-scale asymmetries on the evolution of an idealized vortex similar to the one discussed here. In his idealized experiment, Wang showed that the outer rainbands most frequently form and develop between 80 and 150 km from the TC center. Wang (2009) also showed that the cooling produced in the outer spiral rainbands maintains both the intensity of the tropical cyclone and the compactness of its inner core. However, in our current work the idealized TC did not produce significant outer rainbands. Nevertheless, past works by

Willoughby (1978) and Willoughby et al. (1984), Guinn and Schubert (1993), and Wang (2009) have shown that the dynamics of the outer rainbands differ from the inner rainbands. For instance, Guinn and Schubert (1993) presented evidence that the outer bands form as the result of nonlinear effects during the breakdown of the intertropical convergence zone through barotropic instability. If these rainbands are indeed driven by the larger-scale environment, it is not surprising that the present work with a simplified large-scale environment may not produce significant outer bands. An idealized study that includes some of the complexities of a larger-scale environment and vortex asymmetries may be helpful in understanding the intensity change problem and is proposed as a future work. As the research and operational communities work together under the auspices of NOAA's HFIP to understand the degree to which tropical cyclone intensity forecasts can be improved by increasing the horizontal grid spacing of operational numerical weather prediction (NWP) models, it remains a great challenge for these communities to reach a consensus on vertical resolution and whether the current physics parameterizations in operational NWP models are suitable for horizontal grid spacing of 3 km or smaller. Part II of this work will address some of the above issues.

Acknowledgments. The authors acknowledge funding from the Hurricane Forecast Improvement Project that supported this work. The model was primarily developed at NCEP. The first author wishes to acknowledge several of the scientists at NCEP for their help during the development of this modeling system. The authors acknowledge Dr. Paul Reasor for providing useful comments on improving the original version of this manuscript. Thanks are also due to Gail Derr for offering editorial support. The authors also wish to thank both of the reviewers for providing us with encouraging and insightful comments that led to further improvements of this manuscript.

REFERENCES

Bender, M. A., I. Ginis, R. E. Tuleya, B. Thomas, and T. Marchok, 2007: The operational GFDL coupled hurricane–ocean prediction system and a summary of its performance. *Mon. Wea. Rev.,* **135,** 3965–3989.

Braun, S., and W.-K. Tao, 2000: Sensitivity of high-resolution simulations of Hurricane Bob (1991) to planetary boundary layer parameterizations. *Mon. Wea. Rev.,* **128,** 3941–3961.

Eliassen, A., 1951: Slow thermally or frictionally controlled meridional circulation in a circular vortex. *Astrophys. Norv.,* **5** (2), 19–60.

Emanuel, K. A., 1986: An air–sea interaction theory for tropical cyclones. Part I: Steady-state maintenance. *J. Atmos. Sci.,* **43,** 585–604.

——, 1997: Some aspects of hurricane inner-core dynamics and energetics. *J. Atmos. Sci.,* **54,** 1014–1026.

——, 2003: A century of scientific progress. *Hurricane! Coping with Disaster,* R. Simpson, R. Anthes, and M. Garstang, Eds., Special Publication, Vol. 55, Amer. Geophys. Union, 177–216.

Fierro, A. O., R. F. Rogers, F. D. Marks, and D. S. Nolan, 2009: The impact of horizontal grid spacing on the microphysical and kinematic structures of strong tropical cyclones simulated with the WRF-ARW model. *Mon. Wea. Rev.,* **137,** 3717–3743.

Gopalakrishnan, S. G., and R. Avissar, 2000: LES study of the impacts of land surface heterogeneity on dispersion in the convective boundary layer. *J. Atmos. Sci.,* **57,** 352–371.

——, and Coauthors, 2002: An operational multiscale atmospheric model with grid adaptivity for hurricane forecasting. *Mon. Wea. Rev.,* **130,** 1830–1847.

——, Q. Liu, T. Marchok, D. Sheinin, N. Surgi, R. Tuleya, R. Yablonsky, and X. Zhang, 2010: Hurricane Weather and Research and Forecasting (HWRF) model scientific documentation. NOAA/NCAR/Development Tech Center, 75 pp. [Available online at http://www.dtcenter.org/HurrWRF/users/docs/scientific_documents/HWRF_final_2-2_cm.pdf.]

Gray, W. M., E. Ruprecht, and R. Phelps, 1975: Relative humidity in tropical weather systems. *Mon. Wea. Rev.,* **103,** 685–690.

Guinn, T. A., and W. H. Schubert, 1993: Hurricane spiral bands. *J. Atmos. Sci.,* **50,** 3380–3403.

Hawkins, H. F., and S. M. Imbembo, 1976: The structure of a small, intense hurricane, Inez (1966). *Mon. Wea. Rev.,* **104,** 418–442.

Holland, G. J., 1997: The maximum potential intensity of tropical cyclones. *J. Atmos. Sci.,* **54,** 2519–2541.

Janjić, Z. I., 2003: A non-hydrostatic model based on a new approach. *Meteor. Atmos. Phys.,* **82,** 271–285.

——, J. P. Gerrity Jr., and S. Nickovic, 2001: An alternative approach to nonhydrostatic modeling. *Mon. Wea. Rev.,* **129,** 1164–1178.

Jorgensen, D. P., 1984: Mesoscale and convective scale characteristics of mature hurricanes. Part I: General observations by aircraft. *J. Atmos. Sci.,* **41,** 1268–1285.

Kaplan, J., and M. DeMaria, 2003: Large-scale characteristics of rapidly intensifying tropical cyclones in the North Atlantic basin. *Wea. Forecasting,* **18,** 1093–1108.

——, ——, and J. A. Knaff, 2010: A revised tropical cyclone rapid intensification index for the Atlantic and eastern North Pacific basins. *Wea. Forecasting,* **25,** 220–241.

Kurihara, Y., 1975: Budget analysis of a tropical cyclone simulated in an axisymmetric numerical model. *J. Atmos. Sci.,* **32,** 25–59.

——, and R. E. Tuleya, 1974: Structure of a tropical cyclone developed in a three-dimensional numerical simulation model. *J. Atmos. Sci.,* **31,** 893–919.

Liu, Y., D.-L. Zhang, and M. K. Yau, 1999: A multiscale numerical study of Hurricane Andrew (1992). Part II: Kinematics and inner-core structures. *Mon. Wea. Rev.,* **127,** 2597–2616.

Malkus, J. S., and H. Riehl, 1960: On the dynamics and energy transformations in steady-state hurricanes. *Tellus,* **12,** 1–20.

Marks, F. D., Jr., and R. A. Houze Jr., 1987: Inner core structure of Hurricane Alicia from airborne Doppler radar observations. *J. Atmos. Sci.,* **44,** 1296–1317.

——, ——, and J. F. Gamache, 1992: Dual-aircraft investigation of the inner core of the Hurricane Norbert. Part I: Kinematic structure. *J. Atmos. Sci.,* **49,** 919–942.

Montgomery, M. T., V. S. Nguyen, J. Persing, and R. K. Smith, 2009: Do tropical cyclones intensify by WISHE? *Quart. J. Roy. Meteor. Soc.,* **135,** 1697–1714.

Nguyen, V. S., R. K. Smith, and M. T. Montgomery, 2008: Tropical-cyclone intensification and predictability in three dimensions. *Quart. J. Roy. Meteor. Soc.,* **134,** 563–582.

Ooyama, K. V., 1969: Numerical simulation of the life cycle of tropical cyclones. *J. Atmos. Sci.,* **26,** 3–40.

——, 1982: Conceptual evolution of the theory and modeling of the tropical cyclone. *J. Meteor. Soc. Japan,* **60,** 369–379.

Pan, H.-L., and W.-S. Wu, 1995: Implementing a mass flux convective parameterization package for the NMC Medium-Range Forecast model. NMC Office Note 409, 40 pp. [Available from NOAA/NWS/NCEP/Environmental Modeling Center, WWB, Rm. 207, Washington, DC 20233.]

Pendergrass, A. G., and H. E. Willoughby, 2009: Diabatically induced secondary flows in tropical cyclones. Part I: Quasi-steady forcing. *Mon. Wea. Rev.,* **137,** 805–821.

Riehl, H., 1954: *Tropical Meteorology*. McGraw-Hill, 342 pp.

Ritchie, E. A., J. Simpson, W. T. Liu, J. Halverson, C. Velden, K. F. Brueske, and H. Pierce, 2003: Present day satellite technology for hurricane research. *Hurricane! Coping with Disaster,* R. Simpson, R. Anthes, and M. Garstang, Eds., Special Publication, Vol. 55, Amer. Geophys. Union, 249–289.

Rogers, R., 2010: Convective-scale structure and evolution during a high-resolving simulation of tropical cyclone rapid intensification. *J. Atmos. Sci.,* **67,** 44–70.

Rotunno, R., and K. A. Emanuel, 1987: An air–sea interaction theory for tropical cyclones. Part II: Evolutionary study using a nonhydrostatic axisymmetric numerical model. *J. Atmos. Sci.,* **44,** 542–561.

Shen, W., R. E. Tuleya, and I. Ginis, 2000: A sensitivity study of the thermodynamic environment on GFDL model hurricane intensity: Implications for global warming. *J. Climate,* **13,** 109–121.

Smith, R. K., 1980: Tropical cyclone eye dynamics. *J. Atmos. Sci.,* **37,** 1227–1232.

——, M. T. Montgomery, and S. H. Zhu, 2005: Buoyancy in tropical cyclones and other rotating atmospheric vortices. *Dyn. Atmos. Oceans,* **40,** 189–208.

——, ——, and S. Vogl, 2008: A critique of Emanuel's hurricane model and potential intensity theory. *Quart. J. Roy. Meteor. Soc.,* **134,** 551–561.

——, ——, and N. V. Sang, 2009: Tropical cyclone spin-up revisited. *Quart. J. Roy. Meteor. Soc.,* **135,** 1321–1335.

Sundqvist, H., 1970: Numerical simulation of the development of tropical cyclones with a ten-level model. Part II. *Tellus,* **22,** 504–510.

Tuleya, R. E., and Y. Kurihara, 1975: The energy and angular momentum budgets of a three-dimensional tropical cyclone model. *J. Atmos. Sci.,* **32,** 287–301.

——, and ——, 1978: A numerical simulation of the landfall of tropical cyclones. *J. Atmos. Sci.,* **35,** 242–257.

——, and ——, 1982: A note on the sea surface temperature sensitivity of a numerical model of tropical storm genesis. *Mon. Wea. Rev.,* **110,** 2063–2069.

Wang, Y., 1995: On an inverse balance equation in sigma-coordinates for model initialization. *Mon. Wea. Rev.,* **123,** 482–488.

——, 2002a: An explicit simulation of tropical cyclones with a triply nested movable mesh primitive equations model-TCM3. Part II: Model refinements and sensitivity to cloud microphysics parameterization. *Mon. Wea. Rev.,* **130,** 3022–3036.

——, 2002b: Vortex Rossby waves in a numerically simulated tropical cyclone. Part I: Overall structure, potential vorticity, and kinetic energy budgets. *J. Atmos. Sci.,* **59,** 1213–1238.

——, 2002c: Vortex Rossby waves in a numerically simulated tropical cyclone. Part II: The role in tropical cyclone structure and intensity changes. *J. Atmos. Sci.,* **59,** 1239–1262.

——, 2009: How do outer spiral rainbands affect tropical cyclone structure and intensity? *J. Atmos. Sci.,* **66,** 1250–1273.

Willoughby, H. E., 1978: A possible mechanism for the formation of hurricane rainbands. *J. Atmos. Sci.,* **35,** 838–848.

——, 1979: Forced secondary circulations in hurricanes. *J. Geophys. Res.,* **84,** 3173–3183.

——, 1990a: Temporal changes of the primary circulation in tropical cyclones. *J. Atmos. Sci.,* **47,** 242–264.

——, 1990b: Gradient balance in tropical cyclones. *J. Atmos. Sci.,* **47,** 265–274.

——, 2009: Diabatically induced secondary flows in tropical cyclones. Part II: Periodic forcing. *Mon. Wea. Rev.,* **137,** 822–835.

——, H.-L. Jin, S. J. Lord, and J. M. Piotrowicz, 1984: Hurricane structure and evolution as simulated by an axisymmetric, nonhydrostatic numerical model. *J. Atmos. Sci.,* **41,** 1169–1186.

Yamasaki, M., 1977: A preliminary experiment of the tropical cyclone without parameterizing the effects of cumulus convection. *J. Meteor. Soc. Japan,* **55,** 11–30.

Zhang, D.-L., Y. Liu, and M. K. Yau, 2001: A multiscale numerical study of Hurricane Andrew (1992). Part IV: Unbalanced flows. *Mon. Wea. Rev.,* **129,** 92–107.

Zhang, X., T. S. Quirino, K. S. Yeh, S. Gopalakrishnan, F. D. Marks Jr., and S. B. Goldenberg, 2011: Toward improving hurricane forecast with high resolution model. *Comput. Sci. Eng.,* **13,** 13–21.